Gene-specific endothelial programs drive AVM pathogenesis in SMAD4 and ALK1 loss-of-function

Authors: Dr. Olya Oppenheim[1,2,3], Dr. Wolfgang Giese[1,2], Dr. Hyojin Park[6], Dr. Elisabeth Baumann[1,2,3], Dr. Andranik Ivanov[3,4], Dr. Dieter Beule[3,4], Prof. Anne Eichmann[5,6,7], Prof. Holger Gerhardt[1,2,3,4]

Affiliations:

[1] Max Delbrück Center for Molecular Medicine in the Helmholtz Association, Berlin, Germany

[2] German Center for Cardiovascular Research (DZHK), Partnersite Berlin, Germany

[3] Charité Universitätsmedizin Berlin, Germany

[4] Berlin Institute of Health, Berlin, Germany

[5] Cardiovascular Research Center, Department of Internal Medicine, Yale University School of Medicine, New Haven, CT, USA

[6] Department of Molecular and Cellular Physiology, Yale University School of Medicine, New Haven, CT, USA

[7] PARCC, INSERM, Université de Paris, Paris, France

Short title: **Distinct Endothelial Paths in SMAD4/ALK1 AVMs**

Corresponding author: Prof. Holger Gerhardt (email: Holger.Gerhardt@mdc-berlin.de)

Co-corresponding author: Dr Olya Oppenheim (email: Olya.Oppenheim@mdc-berlin.de)

Max-Delbrück-Center for Molecular Medicine in the Helmholtz Association (MDC)

Robert-Rössle-Strasse 10

13125 Berlin

Germany

Total word count: ~11,152

30 **Non-standard Abbreviations and Acronyms**

AVM	Arteriovenous Malformation
HHT	Hereditary Hemorrhagic Telangiectasia
BMP	Bone Morphogenetic Protein
EC	Endothelial Cell
FSS/LSS/HSS	Fluid/Low/High Shear Stress
siRNA	Small Interfering RNA
siCTRL	Control siRNA
siSMAD4	siRNA against SMAD4
siALK1	siRNA against ALK1
GO_BP	Gene Ontology – Biological Process
DEG	Differentially Expressed Gene
VEGF/VEGFR	Vascular Endothelial Growth Factor/ Vascular Endothelial Growth Factor Receptor
DPP4	Dipeptidyl Peptidase-4
PODXL	Podocalyxin
TEK	TEK Tyrosine Kinase (encodes Tie2)
ENG	Endoglin
ALK1	Activin Receptor-Like Kinase 1 (ACVRL1)
SMAD4	Mothers Against Decapentaplegic Homolog 4
KLF4	Krüppel-like Factor 4
pSMAD159	Phosphorylated SMAD1/5/9
GJA4	Gap Junction Alpha-4 Protein (encodes Connexin 37)
CDKN1B	Cyclin-Dependent Kinase Inhibitor 1B (encodes p27)
NR2F2	Nuclear Receptor Subfamily 2, Group F, Member 2 (encodes COUP-TFII)
DLL4	Delta-Like Ligand 4
HEY1/HEY2	Hairy/Enhancer-of-split related with YRPW motif protein 1/2
ANGPT2	Angiopoietin-2
ColIV	Collagen Type IV
CD31	Cluster of Differentiation 31 (PECAM-1)
ROI	Region of Interest
DABEST	Data Analysis with Bootstrap-Coupled Estimation
HUVEC	Human Umbilical Vein Endothelial Cell
mTmG	Membrane Tomato–Membrane GFP reporter
T-OH	Tamoxifen
PI	Polarity Index
V-score	Signed Polarity Index (for directionality)
NUC/Cyt	Nucleus-to-Cytosol (ratio)
P	Postnatal Day (e.g., P4, P5, P8)

31

Abstract

Background:

Hereditary hemorrhagic telangiectasia is a genetic disorder caused by loss-of-function mutations in components of the bone morphogenetic protein signaling pathway, leading to arteriovenous malformations. Most prior work has treated BMP-component mutations as mechanistically interchangeable, yet whether distinct genes converge on a shared mechanism remains unclear. We aimed to understand the molecular relationship between BMP signaling and endothelial flow response that leads to AVM formation.

Methods:

We expose human endothelial monolayers treated with siRNA against SMAD4 or ALK1 to laminar flow and analyze flow-responsive transcriptomics, flow-responsive BMP signaling activation dynamics, cell polarity and morphology. We analyze the cell-autonomous and non-cell-autonomous migration dynamics of ECs treated with siSMAD4 or siALK1. Using the postnatal mouse retina model, we study EC distribution changes over time in mosaic settings, and assess the remodelling capabilities of Smad4^{iECKO} or Alk1^{iECKO}, relative to littermate controls.

Results:

This study shows that mutations in SMAD4 or ALK1 lead to fundamentally distinct mechanisms of malformation formation. SMAD4 deficiency enhances endothelial responses to blood flow, including transcriptional activation and migration against flow, causing excessive capillary pruning and the development of single large shunts. In contrast, ALK1 deficiency disrupts flow sensing, impairs cell polarization and migration, and promotes a persistent angiogenic state, resulting in dense, hypervascularized networks. RNA sequencing reveals that these transcriptional changes precede flow onset, suggesting early defects in endothelial fate specification. Mosaic in vitro models show that mutant cells co-opt neighboring wild-type cells, while in vivo tracking confirms mutation-specific migration behavior.

Conclusions:

These findings reveal divergent cellular programs driving arteriovenous malformations and underscore the need for gene-specific diagnostic and therapeutic strategies.

Clinical Perspective

What is New?

- This study identifies gene-specific mechanisms of AVM formation in endothelial cells with SMAD4 or ALK1 loss-of-function, two major mutations underlying Hereditary Hemorrhagic Telangiectasia.
- Using multiple side-by-side analyses, the study reveals that SMAD4 deficiency enhances flow-mediated remodeling, while ALK1 deficiency impairs flow sensing and promotes angiogenic persistence.
- RNA sequencing showed that several transcriptional differences precede the onset of flow, indicating early divergence in endothelial cell fate specification and mechanosensory behavior.
- Mosaic culture and retinal models demonstrate that mutant cells exert distinct non-cell-autonomous effects on wild-type endothelial cells.

What Are the Clinical Implications?

- This work challenges the prevailing assumption of a unified pathogenic pathway in HHT and supports a model of mutation-specific AVM pathogenesis, with distinct cellular and molecular drivers.
- The findings provide a mechanistic basis for the variable clinical presentation seen in patients with different HHT mutations.
- Identification of early transcriptional signatures, such as persistent ANGPT2 or DPP4 upregulation, may offer new biomarkers or therapeutic targets for early intervention before AVMs become clinically symptomatic.
- Personalized therapeutic strategies could reduce reliance on invasive treatments and shift toward mechanism-based, precision medicine approaches in HHT and related vascular disorders.

88 **Introduction**

89 The vascular system develops and remodels through a series of complex cellular processes that
90 continuously adapt its shape and function to the local needs of tissues and organs[1–6]. Defects in
91 the fine-tuned coordination of endothelial cell (EC) collective migration, proliferation, perfusion-
92 mediated stabilization and cellular rearrangements in response to fluid shear stress (FSS) can lead
93 to vascular malformations that can severely threaten organ function, or cause bleedings and life-
94 threatening complications. Understanding the precise molecular and cellular mechanisms that
95 drive aberrant vessel formation is fundamental to the development of precision therapy.

96 Central to such understanding is the behavior of ECs during formation and remodeling of the
97 vascular network. Exactly how the collective behavior of ECs leads to the formation of a vascular
98 network with hierarchical organization of arteries, capillaries and veins remains incompletely
99 understood. Whereas the initial vasculogenic assembly of vessels[2,5] and subsequent sprouting
100 angiogenesis[3] are largely independent of blood flow, the stabilization of nascent vessels and the
101 orderly pruning process that leads to the mature network depend on both the biomechanical
102 forces of blood flow and related biochemical signaling events[1,7–14]. Recent work identified flow-
103 migration coupling as the orderly migratory response of ECs to changing FSS which drives
104 functional remodeling. Failure of ECs to engage in this flow-migration coupling process has been
105 shown to occur in animal models of Hereditary Hemorrhagic Telangiectasia (HHT)[7,9,10,15–18].

106 HHT is an autosomal dominant vascular disorder[19], and is characterized by development of
107 arteriovenous malformations (AVMs). Such malformations can occur in many organs and can be
108 small (dilated small blood vessels called telangiectasias, typically appearing on the skin and nasal-
109 mouth mucosa) or large intraorgan AVMs[19,20].

110 The major genetic effectors causing this disorder are part of the Bone Morphogenetic Protein
111 (BMP) signaling pathway[21–24]. Loss-of-function mutations in the co-receptor Endoglin[25], the type
112 I receptor ALK1 and downstream DNA-binding protein SMAD4 account for the majority of
113 diagnosed cases, and lead to HHT1[25], HHT2[26] or JP/HHT[22], respectively.

114 When circulating BMP ligands bind to the extracellular domain of the ALK1-ENG heterotetramer,
115 a conformational change in the intracellular domains subsequently leads to phosphorylation of
116 receptor SMADs 1/5/9. These phosphorylated SMADs then bind to SMAD4 and translocate to the

117 nucleus, where this complex regulates target-gene expression. As homozygous loss-of-function
118 mutations in any of the effectors is embryonic lethal, accumulation of somatic mutations in the
119 healthy allele drives the loss-of-function phenotype, in a process called loss of heterozygosity[23].
120 Shunts appear in a sporadic manner and do not affect the entire vascular network within a tissue.
121 Moreover, different somatic mutations accumulate in different cells and vascular beds[27]. For
122 these shunts to start developing in a mature and quiescent network, a "second hit" vascular
123 injury, which causes a reactivation of the vascular bed and the exit from a quiescent state, is
124 usually required to occur[27,28]. Current treatment options include mostly symptomatic and
125 surgically invasive approaches, while mechanism-based drug options are limited[19,29].
126 The unpredictable behavior, variable presentation, and limited therapeutic options of AVMs pose
127 significant clinical challenges, underscoring the need to elucidate the underlying mechanisms. In
128 our search for critical and common molecular mediators and cellular mechanisms of HHT, we find
129 that loss of SMAD4 or ALK1 surprisingly shows very different effects and influences the EC
130 response to FSS in opposite ways, ultimately leading to different AVM pathomechanisms. Loss of
131 SMAD4 enhances collective migration against flow, leading to hyperpruning of proximal
132 capillaries, therefore precipitating a shunt. In contrast, ALK1 deficient cells show a delayed and
133 reduced migration against flow, coupled with angiogenic persistence, causing AVMs to grow via
134 hypopruning and enlargement of capillaries. These findings provide valuable insights into distinct
135 pathomechanisms that lead to AVM formation, offering potential avenues for improved
136 diagnostics and mechanism based treatment options.
137
138
139
140
141
142
143
144
145

146 ## Methods

147 ### Cell culture experiments

148 Human umbilical venous endothelial cells (HUVECs, PromoCell) were expanded and used in
149 passages 2-4. Culture flasks were coated with 0.2% gelatin prior to seeding. Cells were cultured
150 in EGM2-Bulletkit (Lonza) or MV2 (PromoCell) in a 37°C humidity incubator with 5% CO_2. For
151 siRNA knockdown, cells were seeded in T25 flasks and transfected after 24h at 60-70% confluence
152 for *siCTRL* (Qiagen AllStars negative control, 40pmol), *siSMAD4* (Qiagen, FlexiTube GeneSolution
153 for SMAD4: SI03089527, SI03042508, SI00076041 and SI00076020; 10pmol each) or *siALK1*
154 (Qiagen, FlexiTube GeneSolution for ALK1: SI02659972 and SI02758392, 10pmol each), using
155 RNAiMax transfection reagent (Thermofisher) diluted in OptiMem media and added to antibiotic
156 free EBM2 media (Lonza). After 5h, transfection mix was aspirated and replaced with full media.

157 ### End point flow experiments

158 HUVECs were harvested 24h after siRNA knockdown and seeded onto gelatinized 0.4 Luer
159 ibiTreat slides (Ibidi) at a concentration of 2 million cells per ml and placed overnight in a CO_2
160 incubator. The following day, slides were connected to perfusion units (Ibidi) and exposed to 0.6
161 Pa or 1.8 Pa shear stress for 4h. Cells that were exposed to shear stress for 16h would be
162 connected later on, and would have a media exchange earlier that day. A static control for each
163 condition was placed in the flow incubator for the same duration as the flow experiments. After
164 each flow experiment, cells would either be fixated with 4% PFA for subsequent
165 immunofluorescence assays, or lysed with RLT buffer (RNAeasy RNA extraction kit, Qiagen) for
166 RNA based subsequent analysis.

167 ### RNA extraction for qPCR, RNA seq

168 After flow experiments, cells were lysed with two rounds of 200ul RLT buffer and collected into
169 tubes. Cell lysates were kept in -80°C freezers until all relevant samples have been collected, then
170 RNA extraction would be completed with the RNAeasy kit according to manufacturer's
171 instructions, including DNAse step. RNA concentration was assessed using NanoDrop. RNA was
172 sent to the genomic core facility for RNA sequencing, or used for qPCR analysis. cDNA synthesis

173 was carried out using BioRad's or Thermofisher's cDNA kits according to manufacturer's
174 instructions. qPCR was performed using Taqman probes on a QuantStudio 6 qPCR machine in 384
175 well plates.

176 **Bioinformatic analysis**

177 RNA-Seq reads were mapped to the human genome (GRCh38.p7) using STAR (version 2.7.3a[30]).
178 The reads were assigned to genes with FeatureCounts (version 2.0.3[31]) using Gencode version 25
179 (Ensembl 85) annotation and the following parameters " -t exon -g gene_id -s 2 -p".

180 Differential expression analysis was carried out using DESeq2 (version 1.38[32]) using default
181 parameters. Only genes with at least 5 reads in at least 3 samples were considered for the
182 analysis. Gene set enrichment analysis was carried out with CERNO test from the R tmod package
183 (version 0.50.13[33]) using MsigDB Biological Pathways GO collection.

184 **Immunofluorescence, imaging of *in vitro* flow samples**

185 After fixation, slides were blocked and stained with primary antibodies against VEcadherin (goat,
186 AF938, R&D Systems, 1:1000); GM130 (mouse, 610822, BD Bioscience, 1:500); pSMAD159
187 (rabbit, 13820S, Cell Signaling, 1:500) or KLF4 (rabbit, HPA002926, Sigma Aldrich, 1:500).
188 Secondary antibodies were used in 1:400 dilution: Donkey anti-goat IgG 568 (A11077,
189 Thermofisher); Donkey anti-mouse IgG 488 (A21202, Thermofisher); Donkey anti-rabbit IgG 647
190 (A31573, Thermofisher). Nuclei were stained using a 1:1000 DAPI solution. Mowiol mounting
191 media was mixed with Dabco solution (Sigma) at 10:1 ratio and applied to slides. Slides were
192 imaged on the Zeiss 980 Confocal inverted microscope with a 20x air objective by taking 10 non
193 overlapping z-stack images per slide.

194 **Image analysis of *in vitro* data**

195 Images were processed using sum intensity projection and were then analyzed using the Polarity-
196 JaM toolbox and web-application[34]. The full code is available at https://github.com/polarityjam.
197 Polarity analysis (for nuclei-Golgi polarity, cell orientation) was performed via acquisition of a
198 polarity index (PI), which is an indicator of the concentration of the circular distribution, its value
199 (limited between 0 and 1) indicating the collective orientation strength of the monolayer[35]. In

200 addition, the signed polarity index (V-score) indicates the strength of polarization with respect to
201 a given direction. The signed polarity index varies between -1 and 1 and indicates the strength of
202 polarization with respect to an assumed direction of polarization.

203 Additional features were extracted through the web application www.polarityjam.com:

204 Nuclear marker accumulation was analyzed via the ratio of the mean intensity of
205 pSMAD159/KLF4 in the nucleus and cytosol (NUC/Cyt ratio). Cell area was extracted and
206 normalized to μm^2. Cell elongation was extracted as the major/minor axis ratio. Circular statistics
207 was performed via the PolarityJaM web application. Cell orientation of each condition was
208 extracted as V-score per image from the circular statistics file.

209 **Live migration under flow**

210 For live migration experiments, cells were prepared and seeded in the same conditions as
211 described for the end-point flow experiments. On the day of the experiment, seeding MV2 media
212 was aspirated and replaced with CO2 independent media (Promocell basal media without
213 phenol-red and without sodium bicarbonate, supplemented with MV2 supplement kit, B-
214 glycerolphosphate at a final concentration of 4.32ug/ul and sodium bicarbonate at a final
215 concentration of 0.0075%) with addition of Spy505 (Spyrochrome) nuclear dye at 1:1000 dilution
216 and incubated at 37°C for 4h. Fluidic units would be placed inside the incubation chamber of the
217 microscope and warmed up prior to connection of slides. Slides were connected and placed on
218 multi slide stage insert. Time Lapse imaging would run for 48h and acquire 3x3 tiles with 3 slice
219 Z-stacks for each position, with a time interval of 7.5 minutes. Migration analysis would then be
220 done using the TrackMate feature[36] on Fiji (ImageJ) with StarDist segmentation tool[37]. Tracks
221 would then be analyzed using a Python based script[38] on Jupyter notebook (AnaConda).

222 For mosaic migration experiments, prior to seeding into flow slides, cells were labeled with
223 CellTracker Green or Red (Thermofisher) with 1:5000 dilution (final concentration 2nM) in EBM2
224 media and incubated for 45 minutes in 37°C, then washed three times with full MV2 media and
225 placed in the incubator for about 4h. Cells were then trypsinized and harvested, and seeded in
226 the same concentration with 1:1 ratio between green and red cells. Live imaging would begin the
227 following day, 48h after siRNA treatment. Time Lapse imaging was conFig.d in the same manner,

228 and ran for approx. 2.5 days (500 cycles with 7.5 minute intervals). Subsequent analysis for each
229 channel was done in the same manner as described in the previous paragraph.

230 ***In vivo* experiments**

231 All animal experiments were performed under a protocol approved by the Institutional Animal
232 Care Use Committee of Yale University (no.2023-11406).

233 Seven to eight weeks old ALK1$^{f/f}$ or SMAD4 $^{f/f}$ mice with Cdh5 CreERT2 and mTmG mixed genetic
234 background were intercrossed for experiments and ALK1$^{f/f}$ Cdh5 CreERT2 (mTmG) mice or
235 SMAD4 $^{f/f}$ Cdh5 CreERT2 (mTmG) were used. Gene deletion was induced by intra-gastric
236 injections with 100 µg Tamoxifen (Sigma, T5648; 2.5 mg ml−1) into pups at P4 or P1-3 to stain
237 Collagen type 4 and CD31, and 0.75 µg Tamoxifen into P5 pups for mosaic knockout and labeling.
238 Tx-injected CreERT2 negative littermates were used as controls. Retinae were collected on P6 for
239 Collagen type 4 and CD31 staining, and on P8 and P15 for mosaic population analysis.

240 **Immunostaining and imaging of mouse retinae**

241 Retinae were prefixed in 4% PFA for 8 min at room temperature. Retinae were dissected, blocked
242 for 30 min at room temperature in blocking buffer (1% fetal bovine serum, 3% BSA, 0.5% Triton
243 X-100, 0.01% Na deoxycholate, 0.02% Sodium Azide in PBS at pH 7.4) and then incubated with
244 specific antibodies in blocking buffer overnight at 4C. The next day, retinae were washed and
245 incubated with IB4 together with the corresponding secondary antibody overnight at 4°C, then
246 washed and post-fixed with 0.1% PFA and mounted in fluorescent mounting medium (DAKO,
247 USA). High-resolution pictures were acquired using a Leica SP8 confocal microscope with a Leica
248 spectral detection system (Leica TCS SP8 detector), and the Leica application suite advanced
249 fluorescence software. Primary antibodies: IB4 ([IsolectinB4] #132450, 1:400; Life Technologies),
250 GFP Polyclonal Antibody, Alexa Fluor 488 (#A-21311, 1:1000; Invitrogen), CD31 (553370; 1:200;
251 BD), Collagen IV antibody (2150-1470; 1:400; Bio-Rad).Secondary antibodies: Alexa Fluor 488
252 anti-Rat (A21208, 1:500, Invitrogen), Alexa Fluor 568 anti-Rabbit (A10042, 1:500, Invitrogen).

253

254

255 **Image analysis of *in vivo* data**

256 Analysis of mosaic labeled mouse retinae was done as previously described[39,40]. Briefly, maximum
257 projections of the IB4 channel were used to create drawn masks of retina outline, veins, arteries
258 and optic nerve in Fiji[41]. Maximum projections of the GFP channel were used to create GFP masks.
259 For every pixel in the GFP mask, three numbers were computed (using drawn masks as
260 referential): (1) distance to the nearest vein (d_v); (2) distance to the nearest artery (d_a); and (3)
261 radial distance to the optic nerve (d_r). From these measures, the relative distances by $\phi_{v\text{-}a} = d_v/(d_v$
262 $+ da)$ were obtained. The EC distribution was computed by performing the operation for x
263 randomly selected GFP-positive pixels in each retina, which were used as a proxy for EC
264 distribution. A kernel density estimation was used to approximate the underlying EC distribution
265 in the two-dimensional coordinate system spanned by $\phi_{v\text{-}a}$ and d_r. For computational analysis, a
266 Python-based workflow was used, accessible on GitHub https://github.com/gerhardt-lab/retina-
267 VACS-HHT.

268 Analysis of mouse retinae used in regression analysis was done using the 3DVascNet software[42].
269 Briefly, z-stacks of CD31 and ColIV channels were uploaded into the software, along with a
270 resolution file depicting the micron/pixel ratio of each image. Channels of the same retina were
271 segmented independently from each other. After segmentation, a region of interest (ROI) was
272 selected for each image, generally encompassing one retina leaflet. ROIs are skeletonized in 3D
273 using the generated 3D mask from the segmentation step. The software outputs feature
274 quantifications, including ROI volume and number of branching points. Regression events for
275 each retina are quantified using a composite of the CD31 and ColIV channels and within the
276 borders of the analyzed ROI. A regression event is classified by an absence of the CD31 signal,
277 while ColIV staining remains intact. Partial absence of CD31 indicates the vessel is in an
278 intermediate regression stage; complete absence of CD31 while ColIV staining remains intact
279 indicates the final regression stage of a vessel; complete absence of CD31 and partial disruption
280 of ColIV staining indicates long regressed vasculature. Regression frequency is quantified via the
281 proportion of regression events per 100 branching points in the CD31 channel. Branching points
282 and Vessel density ratios are quantified by dividing the outputs of the CD31 by ColIV channels,
283 and subsequent normalization to the ROI volume ratio.

Statistical Analysis - DABEST method

In order to compute effect sizes along with common p-value statistics, we used the DABEST ('data analysis with bootstrap-coupled estimation') method[43]. The mean difference distributions including 95% confidence intervals were plotted to indicate effect size. Common statistical analysis include two-sided Welch's test, student t-Test and a non-parametric Mann-Whitney test. The test used is indicated in the Fig. captions.

Use of large language models (LLMs)

Large language models (LLMs), including ChatGPT (OpenAI), were used to assist with non-scientific aspects of manuscript preparation, including rephrasing existing text for clarity and readability. In addition, LLMs were used to support the adaptation of existing Python scripts for statistical data analysis, where package updates or deprecated commands required modification. No novel analyses were generated by the model, and all scientific interpretations and data validation were performed by the authors. The updated scripts were added to Github at https://github.com/gerhardt-lab/retina-VACS-HHT.

312 **Results**

313 **RNA sequencing unveils distinct transcriptional regulation associated with ALK1 and SMAD4**
314 **loss-of-function**

315 In search for common pathogenic downstream effectors of ALK1 and SMAD4 loss-of-function we
316 performed RNA sequencing on flow-mediated shear-stress exposed HUVECs following SMAD4 or
317 ALK1 siRNA mediated knock-down (supplementary Fig. 1.1). The FSS magnitude was adjusted to
318 0.6 Pa to simulate FSS values typically occurring in veins and capillaries, as previous work has
319 shown that AVMs in HHT models commence in capillaries and veins, but not in arteries[21]. RNA
320 samples were collected after 4 and 16 hours of flow exposure (Fig. 1a). Principal component
321 analysis (PCA) of all samples showed samples clustered primarily according to flow duration (Fig.
322 1b), with untreated controls (light gray dots) and control siRNA treated samples (dark gray dots,
323 *siCTRL* hereafter) clustering together. Surprisingly however, ALK1 siRNA and SMAD4 siRNA-
324 treated samples did not cluster together. This is remarkable, given that SMAD4 is a downstream
325 component of the BMP9/10 signaling pathway triggered by the activation of ALK1. Instead,
326 *siALK1*-treated samples (magenta dots) clustered separately from *siSMAD4*-treated samples
327 (blue dots), and samples treated with both *siSMAD4* and *siALK1* (siDouble hereafter, green dots),
328 clustered between the two single treatments in all time points. We therefore set out to
329 investigate the differences in gene regulation in more detail.
330 Gene set enrichment analysis using GO biological processes (GO_BP hereafter) directly
331 comparing *siSMAD4*-treated samples versus *siALK1*-treated samples revealed 6 clusters, based
332 on flow dependence and duration (supplementary Fig. 1.2). Flow-dependent GO_BP (Fig. 1c)
333 were divided into 3 clusters - differential expression at early flow exposure (light blue), flow-
334 dependent differential expression (dark blue), and differential expression at late flow exposure
335 (light green). Interestingly, the early and late flow response GO_BP were quite different, with
336 early flow exposure showing an enrichment in upregulation of biological processes associated
337 with cell compartment organization, chemotaxis, VEGF and TGF-beta signaling in *siSMAD4*-
338 treated samples, whereas late flow exposure exhibited enrichment in downregulation of GO_BPs
339 associated with cell fate and arterial differentiation in *siSMAD4* treated samples, compared to
340 *siALK1* treated samples.

341 Evidence plots and volcano plots from the early flow response as well as late flow response
342 exposed many differentially expressed genes, suggesting ALK1 and SMAD4 loss-of-function leads
343 to highly differential effects on the endothelial response to flow (Fig. 1d-e and supplementary
344 Fig. 1.3).

345 **ALK1 is crucial for flow-induced BMP pathway activation, while SMAD4 governs its duration**

346 As SMAD4 is a direct transcriptional regulator of the ALK1-activated BMP pathway but also the
347 TGF-beta pathway, it was essential to understand the roles of both ALK1 and SMAD4 on flow-
348 induced BMP pathway activation. To test this, we exposed HUVECs to low shear stress of 0.6 Pa
349 (LSS hereinafter) for 4 and 16 hours as in the RNAseq setup and assessed BMP pathway activation
350 via the intensity of the nuclear pSMAD159 signal (Fig. 2 a, b). In static conditions, HUVECs
351 displayed basal nuclear pSMAD159 levels. Exposing HUVECs to 4h of LSS showed increased and
352 variable activation of the BMP pathway, which however subsided after 16h in the *siCTRL*-treated
353 samples. The same flow regime in *siSMAD4*-treated samples led to a more uniform activation of
354 the BMP pathway that remained active at 16h, while in *siALK1*-treated samples no flow-induced
355 activation of the BMP pathway was observed. Similar outputs were obtained for high shear stress
356 levels (1.8 Pa, HSS hereinafter, Fig. 2c and supplementary Fig. 2). Taken together, these data
357 suggest an essential role for ALK1 in flow-induced activation of the BMP pathway, while SMAD4
358 absence results in a prolonged, more robust and uniform BMP pathway activation.

359 **SMAD4 and ALK1 deficiency differentially impact cell polarity in endothelial cells**

360 Cell polarity is a crucial aspect of development that is often characterized by the asymmetric
361 distribution of organelles in response to extracellular stimuli such as biophysical forces[44].
362 ECs exhibit a striking ability to establish flow-directed polarity, characterized by the positioning
363 of the Golgi apparatus against the direction of blood flow, during their migratory response[7,9,44].
364 There is growing evidence for changes in this front-rear polarity in AVMs, as well as in ECs
365 depleted of BMP pathway components[21,24]. In order to characterize these changes, we analyzed
366 the nuclei-Golgi polarity of HUVECs after exposure to LSS and HSS for 4 and 16 hours (Fig. 2d-f).
367 In LSS conditions, we observed a weak polarization of *siCTRL*-treated samples against flow
368 direction at 4h which reversed and intensified at 16h (Fig. 2 d, e). Surprisingly, *siSMAD4*-treated

369 samples polarized against flow direction in both time points, whereas *siALK1*-treated samples
370 exhibited random polarization at 4h, followed by a weak polarization with flow at 16h. When
371 exposed to HSS, cells polarized against flow in all treatments although with strongest effects in
372 *siSMAD4*-treated samples (Fig. 2 d, f). The fact that even *siALK1*-treated samples polarize against
373 flow, although they do not show induction of pSMAD1/5/9, suggests that polarization induced
374 by HSS occurs independent of BMP pathway activation. In summary, our data shows that ECs
375 lacking SMAD4 or ALK1 respond very differently to FSS, particularly under LSS levels.

376 **FSS-dependent changes in cellular morphology are enhanced in the absence of SMAD4**

377 A key function of flow-migration coupling of ECs is the fine tuning of vessel diameter. This fine
378 tuning depends on the ability of ECs to accurately sense flow and to undergo cellular
379 rearrangements that affect their morphology, size and orientation. Our data demonstrate that
380 *siALK1*-treated samples fail to upregulate BMP signaling and to polarize against flow at LSS levels,
381 suggesting they might have either lost the ability to sense flow, or to respond to flow. The
382 expression of Krüppel-like 4 (KLF4) transcription factor has been established as flow
383 sensitive[11,45,46], as its mRNA levels increase in ECs upon exposure to flow. Analysis of KLF4
384 expression as surrogate for flow sensitivity confirmed that ECs sense the exposure to FSS under
385 the different siRNA knockdown conditions. *siCTRL*- and *siSMAD4*-treated samples showed
386 elevated KLF4 expression upon LSS exposure, and also *siALK1*-treated samples showed elevated
387 KLF4 expression, albeit to a significantly lower magnitude (Fig. 3a). The notion that lack of ALK1
388 or SMAD4 differentially affects transcriptional responses to flow is further supported by the
389 evidence plot of the biological process "Response to fluid shear stress" (Fig. 3b).
390 Immunofluorescence staining for KLF4 protein also confirmed increased protein accumulation in
391 the nucleus upon exposure to LSS. Albeit not to the same degree as seen at RNA level, *siSMAD4*-
392 treated samples had elevated nuclear KLF4 accumulation in both time points (Fig. 3c,
393 supplementary Fig. 3a). In addition, we stained ECs for the adherens junction marker VE-
394 Cadherin, allowing us to segment and analyze cell area, elongation and orientation and evaluate
395 which of these are flow-dependent and/or dependent on the loss of ALK1 or SMAD4 (Fig. 3d-g,
396 supplementary Fig. 3b-e). Already in static conditions and throughout the flow experiment,
397 *siALK1*-treated ECs in the monolayer formed distinct swirl-like clusters, where each sub-

398 population maintained unique orientations independent of neighboring clusters (Supplementary
399 Fig. 3b). After 16h of LSS, the cell area of *siALK1*-treated ECs remained similar to *siCTRL*-treated
400 ECs (Fig. 3f, supplementary Fig. 3c). Although they were significantly more elongated (Fig. 3g),
401 the elongation of *siALK1*-treated ECs was flow independent (Supplementary Fig. 3d). In contrast,
402 *siSMAD4*-treated ECs had a significantly larger cell area compared to *siCTRL*- and *siALK1*-treated
403 ECs (Fig. 3f, supplementary Fig. 3c). In addition, *siSMAD4*-treated ECs elongated and oriented
404 themselves in a flow dependent manner (Fig. 3e,g and supplementary Fig. 3d,e). Taken together,
405 these observations further suggest an enhanced sensitivity to LSS in absence of SMAD4 and
406 reduced sensitivity to LSS in case of ALK1 absence.

407 **Endothelial cells exhibit distinct migration patterns in the absence of ALK1 or SMAD4**

408 The end point analyses of SMAD4 and ALK1 deficient ECs so far captured two distinct phenotypes
409 that suggest hypersensitivity and hyposensitivity to LSS, respectively. We therefore hypothesized
410 that *siSMAD4*-treated ECs would migrate faster against flow, while *siALK1*-treated ECs would
411 migrate less effectively against flow. By labeling the nuclei of ECs and tracking their movement
412 over time under LSS conditions, we were able to analyze the migration pattern of ECs under
413 different siRNA-treatment conditions (Fig. 4a-c, supplementary movies 1a-c). Analysis of
414 individual cell tracks as well as population behaviour revealed that *siCTRL*-treated ECs exhibit a
415 mild preference to migrate against flow (Fig. 4a, b left panels, red tracks), with a smaller
416 proportion of cells migrating with flow (blue tracks) or perpendicular to flow. *siSMAD4*-treated
417 ECs exhibited a much more prominent shift in trajectories against flow direction and also less
418 perpendicular trajectories. The fraction of cells migrating with flow was reduced, but surprisingly,
419 they moved with higher velocities (Fig. 4a, b middle panels). *siALK1*-treated ECs also showed an
420 increased velocity as well as overall cell movement, but with the majority of cells migrating with
421 flow. (Fig. 4a, b right panels). Plotting the average migration of all cells parallel to flow for each
422 condition, revealed that *siCTRL*-treated ECs initially migrate against flow, then reverse direction
423 to move with flow, and ultimately slow down to cease migrating after 48h. *siSMAD4*-treated ECs
424 show a higher acceleration in net migration velocity against flow, but continue to migrate against
425 flow throughout the duration of the experiment. *siALK1*-treated ECs initially behave similar to
426 *siCTRL*-treated ECs, but rapidly decrease net migration velocity parallel to flow (Fig. 4c top panel).

427 Intriguingly, *siCTRL*-treated cells show an average total velocity (irrespective of direction) that is
428 slower than that of cells of the other conditions. *siALK1*-treated ECs show the highest initial
429 velocity and slow down over time to match the speed of *siSMAD4*-treated ECs, but unlike the
430 latter, they fail to migrate directionally against flow. These data strengthen the hypothesis that
431 loss of SMAD4 renders ECs hypersensitivity to flow as they migrate more effectively against flow,
432 while the loss of ALK1 leaves ECs unable to collectively respond to shear stress as they fail to
433 migrate against flow, despite their high migratory potential. *siCTRL*-treated ECs display a very
434 characteristic biphasic response and strong flow adaptation, suggesting that the rearrangements
435 of ECs as a consequence of shear stress represent a transitory adaptation mechanism.
436 As HHT progresses by the loss of heterozygosity via somatic mutations on the healthy alleles of
437 BMP pathway components in a subset of endothelial cells within a vascular plexus, a model for
438 cell migration that more closely resembles the *in vivo* situation of HHT would be a mosaic scenario
439 where only a subset of cells is deficient for SMAD4 or ALK1. By separately labeling the two
440 populations, we generated and observed these mosaic scenarios under flow (Fig. 4d-g,
441 supplementary movies 2a-c). Intriguingly, in the mosaic situation, when *siSMAD4*-treated cells
442 were cultured together with *siCTRL*-treated cells, the latter group migrated more effectively
443 against flow (Fig. 4e-middle panels and 4f-blue curve), initially without elevation of their overall
444 average velocity, following the migration pattern of *siSMAD4*-treated cells; Interestingly, the
445 overall average velocity of *siCTRL*-treated cells increased later on (Fig. 4g-blue curve). The
446 opposite was observed when *siCTRL*-treated cells were cultured with *siALK1*-treated cells, as
447 *siCTRL*-treated cells exhibited a noticeable shift towards migrating with the direction of flow,
448 resulting in an average migration velocity of 0µm/h (Fig. 4e right panel and 4f-pink curve).
449 Interestingly, this mosaic condition overcame the initial delay and displayed elevated migration
450 against flow starting from the second day, preceding the *siCTRL*-mosaic condition by 10h. Taken
451 together, these findings suggest that the absence of SMAD4 not only results in cell-autonomous
452 hypersensitivity to LSS, but also that these cells affect control cells to migrate in a similar fashion.
453 Likewise, the absence of ALK1 results in a cell-autonomous hyposensitivity of ECs to FSS, and also
454 a non-cell autonomous effect on the co-migration of control cells in the mosaic situation.
455

456 **Cells lacking Alk1 or Smad4 exhibit distinct population movements in the retina *in vivo***

457 Should the loss of ALK1 or SMAD4 affect EC migration patterns in a similar way *in vivo*, we would
458 predict that ALK1 knock-out ECs show a mild inability to migrate against flow, whereas SMAD4
459 knock-out cells migrate even more effectively than control cells. To assess this possibility, we
460 turned to the mouse retina model, and employed mosaic endothelial Cre-lox mediated genetic
461 labelling to follow population movements over time. Using our bespoke dual coordinate EC
462 distribution analysis[39,40], we tracked the changes in EC population positions in mosaic retinae
463 overtime. CDH5-Cre^{ERT2} mTmG (CTRL^{mTmG} hereinafter), CDH5-Cre^{ERT2} Smad4$^{fl/fl}$ mTmG
464 (Smad4^{mTmG} hereinafter) or CDH5-Cre^{ERT2} Acvrl1$^{fl/fl}$ mTmG (Alk1^{mTmG} hereinafter) pups were
465 treated with a low dose (0.75ug) of Tamoxifen at P5, to induce mosaic knockout of Smad4 or
466 Alk1, respectively (Fig. 5a). Retinae were collected at P8 and P15 and stained for GFP and IB4 (Fig.
467 5a-b). Using this approach, we have previously shown that EC populations shift from the vein and
468 plexus to the artery, as cells migrate against the direction of flow[39,40]. The GFP+ EC density within
469 the artery and surrounding arterioles was slightly reduced for Smad4^{mTmG} and Alk1^{mTmG} retinae at
470 P8 relative to CTRL^{mTmG} (supplementary Fig. 4b-d – left; Fig. 5c – P8 KDE plots). Between P8 and
471 P15 CTRL^{mTmG} retinae showed a prominent shift of cells to the artery (position 1.0 in the KDE plots
472 at Fig. 5c, Fig. 5d – gray plots). However, this was even more pronounced in the Smad4^{mTmG}
473 retinae (Fig. 5c-d, blue plots), but much less so in Alk1^{mTmG} retinae (Fig. 5c-d, pink plots). Further
474 analysis of GFP+ ECs on the vein-artery axis confirmed a significant shift out of the peri-venous
475 capillary bed for Smad4^{mTmG} as well as a shift into the peri-arterial capillary bed (Fig. 5e-f, blue
476 plots). Alk1^{mTmG} retinae exhibit a weak shift within the peri-venous capillary bed, as well as a mild
477 shift towards the peri-arterial capillaries and arteries, but insignificantly relative to control and
478 much less than Smad4 mutant cells (supplementary Fig. 4c, pink plots, Fig. 5e-f, pink plots).
479 Overall, these results demonstrate that mosaic loss of Smad4 or Alk1 in ECs *in vivo* leads to
480 differential migration defects, in line with our observations in the *in vitro* flow assays. Whereas
481 the absence of Smad4 enhances directional migration towards arterial structures, the absence of
482 Alk1 seems to impair this directional EC migration, but not completely prevent it.
483

484 **Loss of Smad4 leads to hyper-pruning, while loss of Alk1 causes hyper-sprouting during AVM**
485 **formation *in vivo***

486 Directional migration from vein to artery has been identified as the driving mechanism for
487 pruning of the capillary plexus during vascular remodelling[47,48]. We therefore hypothesized that
488 the loss of Smad4 should trigger hyperpruning, hence increased capillary regression. In contrast,
489 reduced sensitivity and propensity to migrate against flow, as seen in Alk1 deficient ECs, should
490 rather trigger hypopruning, causing a hyperdense plexus. In order to analyze the regression
491 frequencies in the postnatal retinal vasculature of both Smad4 knockout (Smad4^{iECKO} hereinafter)
492 and Alk1 knockout (Alk1^{iECKO} hereinafter), we performed immunofluorescent labeling using
493 antibodies against CD31 and collagen type IV (ColIV) to visualize ECs and the vascular basement
494 membrane, respectively (Fig. 6a-b). While Smad4^{iECKO} retinae overall showed a similar regression
495 frequency to its littermate control (Fig. 6c - left, 6d – blue bars), we observed a decrease in the
496 branching points density (Fig. 6e – blue bars), indicating elevated vessel regression at earlier time
497 points. In contrast, we observed a significant reduction in regression frequency in Alk1^{iECKO}
498 retinae (Fig. 6c - right, 6d – pink bars), together with increase in branching points density as well
499 as vessel density (Fig. 6e-f). In addition, Alk1^{iECKO} retinae exclusively exhibited an overall increase
500 in sprouting frequency, which was also visible within the AVM region (Fig. 6c, cyan triangles and
501 supplementary Fig. 5). These results further support our hypothesis that Smad4 deletion and Alk1
502 deletion differentially affect remodelling of the vascular plexus.

503 **Discussion**

504 This study identifies distinct molecular and cellular mechanisms underlying AVM formation in ECs
505 with SMAD4 and ALK1 loss-of-function. Our findings highlight that while both SMAD4 and ALK1
506 loss-of-function contribute to AVM pathogenesis, the underlying cellular behaviors and
507 transcriptomic responses differ markedly, pointing to divergent mechanisms driving these
508 vascular pathologies.
509 The results reveal that SMAD4 loss-of-function enhances EC sensitivity to LSS, leading to
510 increased hypertrophy and directional migration. The observed increase in KLF4 expression upon
511 SMAD4 deficiency confirms recent findings[24], lending strength to the concept that AVM

512 formation is primarily driven by changes in EC mechanotransduction[49]. The combined effects of
513 increasing cell size, a phenotype first reported in ENG mutants in zebrafish[50], and our unique
514 observation of increased directional migration, orientation and polarization against flow, suggest
515 an intriguing pathomechanism: this heightened migratory response accelerates vascular
516 remodelling, resulting in premature capillary regression and the formation of large, high-flow AV
517 shunts. Such a mechanism would explain the distinct appearance of AVMs in SMAD4 mutant
518 retinae. Our data provide several levels of evidence for increased flow sensitivity in SMAD4
519 deficient ECs: First, transcriptional changes highlight besides classical flow-responsive genes like
520 KLF4 and KLF2, also prominent flow-regulated upregulation of cell surface proteoglycans involved
521 in endothelial permeability regulation and vessel lumen regulation, like PODXL[51–54]
522 (Supplementary Fig. 1.3a). Second, flow-mediated cell shape changes and directional polarity are
523 surprisingly enhanced rather than diminished in the absence of SMAD4 (Figs 2 and 3). Third,
524 directional EC population movements both *in vitro* (Fig. 4) and *in vivo* identify increased
525 movement towards the artery, a behaviour depending on flow-responses[9] (Fig. 5). The cause for
526 such enhanced flow sensitivity in SMAD4-deficient ECs remain to be identified.
527 One possibility is that ALK1 and SMAD4 differentially tune endothelial sensitivity to pro-
528 angiogenic versus remodelling cues. Recent work by Franco and colleagues' identified
529 competition between the chemotactic gradient of VEGFA and the mechanical directional
530 response due to flow[7]. Conceptually, this competition plays out in the capillary transition zone
531 where VEGFA gradients and flow gradients compete. Intriguingly, both processes involve VEGFR
532 signaling, with evidence for ligand-independent activation of VEGFR2 by flow, versus ligand-
533 dependent activation in the context of sprouting. Furthermore, Notch signaling is linked to
534 controlling arterial and venous cell fate acquisition[55,56], sprouting[57] as well as flow-induced
535 remodelling[58–60]. Thus, the loss of ALK1 may drive hypersprouting and venous/capillary
536 overgrowth by reduced Notch and increased ligand-dependent VEGFR2 signalling, whereas the
537 loss of SMAD4 selectively enhances Notch related pruning through flow-dependent VEGFR2
538 mechanisms. In line with this idea, GO term analysis highlights a consistent pattern of
539 transcriptional dysregulation in VEGFR signaling and Integrin mediated cell adhesion in *siSMAD4*-
540 treated ECs relative to *siALK1*-treated ECs (Fig. 1c, d and supplementary Fig. 1.2, 1.3): Gene sets

541 involved in negative regulation of VEGFR signaling (M22989, M25085) show predominant
542 upregulation of their constituent genes, while positive regulators (M15928) exhibit
543 downregulation. In addition, GO terms related to integrin-mediated cell adhesion showed a
544 predominance of upregulated genes (M23222, M23221, M13232). These data suggest a
545 transcriptional reprogramming that may reduce VEGFR2 pathway activity, potentially altering
546 cellular responses to flow stimuli. As VEGFR2 activation can occur via ligand-dependent (VEGF-A-
547 mediated) or ligand-independent (flow-induced) mechanisms[61], shifts in the expression of key
548 regulatory genes may influence the dominant signaling mode. In *siSMAD4*-treated cells, DPP4
549 and PODXL were enriched as part of integrin-mediated cell adhesion GO Terms, and were
550 uniquely upregulated - DPP4 in a flow-independent manner, and PODXL in a flow-dependent
551 manner, relative to both *siCTRL*- and *siALK1*-treated cells (Fig. 1d, Supplementary Fig. 1.3a, b).
552 Both genes are implicated in modulating endothelial adhesion and migration[53,62,63], and may
553 contribute to the altered flow responsiveness observed. DPP4 in particular, has been linked to
554 endothelial-to-mesenchymal transition (EndMT) through a TGF-β2-dependent, SMAD-
555 independent mechanism[64]. Its interaction with integrin β1 has been shown to upregulate VEGFR1
556 expression, which acts as a decoy receptor and suppresses VEGFR2 signaling. In parallel, we
557 observed downregulation of ITGAV and ITGB3 – integrins that facilitate VEGF-A binding and
558 ligand-dependent VEGFR2 activation (Supplementary Fig.1.3c,d)[65]. This combination suggests a
559 shift away from VEGF-A-dependent signaling and toward ligand-independent, flow-induced
560 VEGFR2 activation, which may underlie the enhanced sensitivity to flow observed in SMAD4-
561 deficient ECs. However, further experimental validation is required to confirm these regulatory
562 mechanisms and their functional consequences.
563 This molecular shift is mirrored in the striking vascular phenotype observed *in vivo*. SMAD4 loss-
564 of-function in the postnatal mouse retina leads to large shunts devoid of a surrounding capillary
565 plexus. Yet, even the peripheral plexus that will be hypoxic, showing upregulation of hypoxia
566 induced genes, like ANGPT2[66], shows no sign of hypersprouting, unlike in the case of ALK1 mutant
567 conditions. Thus, the lack of SMAD4 appears to selectively increase endothelial responses to flow,
568 whilst reducing endothelial responses that are normally triggered by hypoxia. This phenotypic
569 divergence reinforces the notion that SMAD4 plays a key role in balancing competing angiogenic

570 cues and may act as a molecular switch between sprouting- and flow-mediated endothelial
571 programs.
572 In contrast, ALK1 loss-of-function appears to impair endothelial sensitivity to LSS, disrupting
573 vascular remodelling and leading to reduced capillary regression (Fig. 6). We observed a blunted
574 upregulation of KLF4 and diminished responses to LSS across multiple parameters, including
575 reduced polarization, orientation (Fig. 2,3) and migration of ALK1-deficient cells both *in vitro* and
576 *in vivo* (Fig. 4,5). This remodelling failure results in hypervascularized networks with dense, multi-
577 capillary AVMs (Fig. 6d–f). While directional migration is impaired, it does not appear to be the
578 primary mechanism driving AVM formation: in mosaic monolayers under flow, *siALK1* cells show
579 reduced directional migration during the first half of the experiment. However, in the second
580 half, both *siCTRL* and *siALK1* populations migrate against the flow direction - doing so even earlier
581 than cells in *siCTRL*-mosaic cultures. Similarly, in mosaic retinae, ALK1-deficient GFP^+ ECs still
582 migrate toward the artery, albeit less efficiently. These findings indicate that although ALK1
583 deficiency delays flow-induced migration, it does not completely abolish the endothelial capacity
584 to migrate in response to mechanical cues.
585 Instead, our transcriptional data point to a more fundamental defect in endothelial fate
586 specification and quiescence that arises prior to flow onset. ALK1-deficient ECs already show
587 downregulation of key fate regulators, including the arterial markers GJA4 (Connexin37) and
588 CDKN1B (p27) (Supplementary Fig. 1.3e,f)[55], as well as the venous markers BMP4[8] and NR2F2
589 (COUP-TFII)((Supplementary Fig. 1.3g,h)[56,67]. In addition, Notch signaling appears uncoupled
590 from flow stimuli: canonical Notch targets DLL4, HEY1, and HEY2 do not respond appropriately
591 under shear stress, particularly at 4h (Supplementary Fig. 1.3i-k). These early changes coincide
592 with persistent ANGPT2 upregulation (Supplementary Fig. 1.3l) and downregulation of its
593 receptor TEK (Tie2) (Supplementary Fig.1.3m), even before the onset of flow. Given that ANGPT2
594 is a potent pro-angiogenic factor normally suppressed under flow to promote quiescence[68,69],
595 this pattern suggests that ALK1-deficient ECs remain in an immature, angiogenic-like state –
596 unable to transition into a flow-responsive phenotype. Our findings are supported by recent work
597 in ALK1-null hiPSC-derived ECs, where ANGPT2 upregulation and reduced pSMAD1/5/9 signaling
598 similarly marked a persistent angiogenic state[70].

599 While previous studies comparing phenotypes and pathomechanisms of AVM formation
600 between SMAD4, ALK1 and ENG mutants highlighted similarities, including upregulation of
601 ANGPT2[71], we only find ANGPT2 upregulation in ALK1 deficient cells, in line with the notion of
602 failed induction of quiescence[68,72]. A possible reason for this apparent discrepancy is the fact that
603 we analyzed cell-autonomous gene regulation in ECs under flow, in the absence of pathology.
604 Once an AVM has formed *in vivo*, studying altered gene regulation will report changes that may
605 be primary, but also changes that are secondary to the altered tissue environment, including
606 hypoxia. ANGPT2 is a canonical marker of endothelial activation by hypoxia, but also in
607 inflammatory conditions[69,73]. The fact that large areas of the endothelium upregulate ANGPT2 in
608 bulk RNAseq of isolated ECs from Smad4 mutant retinae[66], like those from Alk1 mutant retinae,
609 is not necessarily evidence for a common causative ANGPT2-induced pathomechanism.
610 Nevertheless, ANGPT2 overexpression may contribute as a driver of wider tissue responses in
611 both conditions.
612 Our findings challenge the notion that AVM formation in SMAD4 and ALK1 loss-of-function
613 follows a unified pathway. Instead, they support a model in which SMAD4 loss-of-function
614 promotes FSS-driven vascular remodelling, while ALK1 loss-of-function primarily disrupts cell fate
615 acquisition and exit from an angiogenic state. These insights align with prior studies implicating
616 BMP signaling dysregulation in AVM pathogenesis[26,57,74], but also highlight the necessity of
617 pathway-specific therapeutic strategies.
618 This study opens several avenues for future research. The observed differences in transcriptional
619 and behavioral responses between SMAD4 and ALK1 loss-of-function highlight the need for
620 further mechanistic studies using multi-omics approaches. Combining transcriptomics,
621 proteomics, and single-cell analyses across various tissue contexts could clarify which signaling
622 effectors are primary drivers of AVM formation versus secondary responses to established
623 pathology. Additionally, exploring factors such as ANGPT2 in ALK1 loss-of-function and DPP4 in
624 SMAD4 loss-of-function could uncover novel targets for modulating EC behavior.
625 In conclusion, this work provides a mechanistic framework for understanding AVM pathogenesis
626 and underscores the need for pathway-specific therapeutic strategies in addressing vascular
627 anomalies such as HHT.

Acknowledgements

We thank Leducq ATTRACT network members Hemaxi Narotamo and Claudio Franco, Douglas Marchuk, David Hardman and Miguel Bernabeu for providing ongoing support throughout this project, as well as Tatiana Borodina, Eireen Bartels-Klein, Irene Hollfinger for technical assistance and guidance.

Disclosures

This manuscript includes results of the doctoral thesis entitled "Distinct endothelial pathomechanisms drive arteriovenous malformations in ALK1 or SMAD4 loss-of-function conditions" submitted by Olya Oppenheim to the faculty of Charité Universitätsmedizin Berlin in 2025.

Author contributions

Olya Oppenheim: Conceptualization; data curation; formal analysis; investigation; methodology; software; project administration; validation; visualization; writing – original draft; writing – review and editing.

Wolfgang Giese: Formal in vitro analysis; methodology; software; visualization; writing – review and editing.

Hyojin Park: In vivo data curation; investigation; methodology; validation; writing – review.

Elisabeth Baumann: Formal in vivo analysis; methodology; software; visualization.

Andranik Ivanov: Computational analysis of the transcriptomic data; methodology; writing – review and editing.

Dieter Beule: Project administration; funding acquisition.

Anne Eichmann: Conceptualization; funding acquisition; investigation; writing – review.

Holger Gerhardt: Conceptualization; investigation; funding acquisition; supervision; project administration; writing – review and editing.

Data Accessibility.

The raw RNA-Seq reads are deposited in the GEO database under accession number GSE282952.

654 Funding

655 This work was supported by the Deutsches Zentrum für Herz-Kreislaufforschung, the
656 Bundesministerium für Bildung und Forschung, the Deutsche Forschungsgemeinschaft by grant
657 number 329389797, CRC1444 and CRC1470. This project has also been supported through grants
658 from the Fondation Leducq (17 CVD 03; TNE ATTRACT, A.E) and NIH (R01 HL169510, A.E and
659 M.A.S).

660

661 **References**

662 1. Geudens, I. & Gerhardt, H. Coordinating cell behaviour during blood vessel formation. *Dev. Camb.*
663 *Engl.* **138**, 4569–4583 (2011).
664 2. Goldie, L. C., Nix, M. K. & Hirschi, K. K. Embryonic vasculogenesis and hematopoietic specification.
665 *Organogenesis* **4**, 257–263 (2008).
666 3. Adair, T. H. & Montani, J.-P. Overview of Angiogenesis. in *Angiogenesis* (Morgan & Claypool Life
667 Sciences, 2010).
668 4. Xu, K. & Cleaver, O. Tubulogenesis during blood vessel formation. *Semin. Cell Dev. Biol.* **22**, 993–
669 1004 (2011).
670 5. Risau, W. & Flamme, I. Vasculogenesis. *Annu. Rev. Cell Dev. Biol.* **11**, 73–91 (1995).
671 6. Ricard, N. & Simons, M. When It Is Better to Regress: Dynamics of Vascular Pruning. *PLOS Biol.* **13**,
672 e1002148 (2015).
673 7. Barbacena, P. *et al.* Competition for endothelial cell polarity drives vascular morphogenesis in the
674 mouse retina. *Dev. Cell* **57**, 2321-2333.e9 (2022).
675 8. Chavkin, N. W. *et al.* Endothelial cell cycle state determines propensity for arterial-venous fate. *Nat.*
676 *Commun.* **13**, 5891 (2022).
677 9. Lee, H.-W., Shin, J. H. & Simons, M. Flow goes forward and cells step backward: endothelial
678 migration. *Exp. Mol. Med.* **54**, 711–719 (2022).

679 10. Roux, E., Bougaran, P., Dufourcq, P. & Couffinhal, T. Fluid Shear Stress Sensing by the Endothelial
680 Layer. *Front. Physiol.* **11**, 861 (2020).
681 11. Moonen, J.-R. *et al.* KLF4 recruits SWI/SNF to increase chromatin accessibility and reprogram the
682 endothelial enhancer landscape under laminar shear stress. *Nat. Commun.* **13**, 4941 (2022).
683 12. Tzima, E., Kiosses, W. B., del Pozo, M. A. & Schwartz, M. A. Localized Cdc42 Activation, Detected
684 Using a Novel Assay, Mediates Microtubule Organizing Center Positioning in Endothelial Cells in
685 Response to Fluid Shear Stress*. *J. Biol. Chem.* **278**, 31020–31023 (2003).
686 13. Tzima, E. *et al.* Activation of Rac1 by shear stress in endothelial cells mediates both cytoskeletal
687 reorganization and effects on gene expression. *EMBO J.* **21**, 6791–6800 (2002).
688 14. Edgar, L. T. *et al.* Traffic Patterns of the Migrating Endothelium: How Force Transmission Regulates
689 Vascular Malformation and Functional Shunting During Angiogenic Remodelling. *Front. Cell Dev.*
690 *Biol.* **10**, 840066 (2022).
691 15. Baeyens, N. *et al.* Vascular remodeling is governed by a VEGFR3-dependent fluid shear stress set
692 point. *eLife* **4**, e04645.
693 16. Georgieva, P. B., Marchuk, D. A., Gerhardt, H., & Leducq ATTRACT Consortium*. ATTRACT. *Circ. Res.*
694 **125**, 262–264 (2019).
695 17. Lee, H.-W. *et al.* Role of Venous Endothelial Cells in Developmental and Pathologic Angiogenesis.
696 *Circulation* **144**, 1308–1322 (2021).
697 18. Rosa, A. *et al.* WASp controls oriented migration of endothelial cells to achieve functional vascular
698 patterning. *Development* **149**, dev200195 (2022).
699 19. Grigg, C., Anderson, D. & Earnshaw, J. Diagnosis and Treatment of Hereditary Hemorrhagic
700 Telangiectasia. *Ochsner J.* **17**, 157–161 (2017).
701 20. Arthur, H. M. & Roman, B. L. An update on preclinical models of hereditary haemorrhagic
702 telangiectasia: Insights into disease mechanisms. *Front. Med.* **9**, 973964 (2022).

703 21. Park, H. *et al.* Defective Flow-Migration Coupling Causes Arteriovenous Malformations in Hereditary
704 Hemorrhagic Telangiectasia. *Circulation* **144**, 805–822 (2021).
705 22. Ola, R. *et al.* SMAD4 Prevents Flow Induced Arteriovenous Malformations by Inhibiting Casein
706 Kinase 2. *Circulation* **138**, 2379–2394 (2018).
707 23. Snellings, D. A. *et al.* Somatic Mutations in Vascular Malformations of Hereditary Hemorrhagic
708 Telangiectasia Result in Bi-allelic Loss of ENG or ACVRL1. *Am. J. Hum. Genet.* **105**, 894–906 (2019).
709 24. Banerjee, K. *et al.* SMAD4 maintains the fluid shear stress set point to protect against arterial-
710 venous malformations. *J. Clin. Invest.* **133**, e168352 (2023).
711 25. Jin, Y. *et al.* Endoglin prevents vascular malformation by regulating flow-induced cell migration and
712 specification through VEGFR2 signalling. *Nat. Cell Biol.* **19**, 639–652 (2017).
713 26. Corti, P. *et al.* Interaction between alk1 and blood flow in the development of arteriovenous
714 malformations. *Development* **138**, 1573–1582 (2011).
715 27. DeBose-Scarlett, E. *et al.* Somatic mutations in arteriovenous malformations in hereditary
716 hemorrhagic telangiectasia support a bi-allelic two-hit mutation mechanism of pathogenesis. *Am. J.*
717 *Hum. Genet.* **111**, 2283–2298 (2024).
718 28. Bernabeu, C., Bayrak-Toydemir, P., McDonald, J. & Letarte, M. Potential Second-Hits in Hereditary
719 Hemorrhagic Telangiectasia. *J. Clin. Med.* **9**, 3571 (2020).
720 29. Robert, F., Desroches-Castan, A., Bailly, S., Dupuis-Girod, S. & Feige, J.-J. Future treatments for
721 hereditary hemorrhagic telangiectasia. *Orphanet J. Rare Dis.* **15**, 4 (2020).
722 30. Dobin, A. *et al.* STAR: ultrafast universal RNA-seq aligner. *Bioinformatics* **29**, 15–21 (2013).
723 31. Liao, Y., Smyth, G. K. & Shi, W. featureCounts: an efficient general purpose program for assigning
724 sequence reads to genomic features. *Bioinformatics* **30**, 923–930 (2014).
725 32. Love, M. I., Huber, W. & Anders, S. Moderated estimation of fold change and dispersion for RNA-seq
726 data with DESeq2. *Genome Biol.* **15**, 550 (2014).

727 33. Zyla, J. *et al.* Gene set enrichment for reproducible science: comparison of CERNO and eight other
728 algorithms. *Bioinformatics* **35**, 5146–5154 (2019).
729 34. Giese, W. *et al.* Polarity-JaM: an image analysis toolbox for cell polarity, junction and morphology
730 quantification. *Nat. Commun.* **16**, 1474 (2025).
731 35. Topics in Circular Statistics | Series on Multivariate Analysis.
732 https://www.worldscientific.com/worldscibooks/10.1142/4031.
733 36. Ershov, D. *et al.* TrackMate 7: integrating state-of-the-art segmentation algorithms into tracking
734 pipelines. *Nat. Methods* **19**, 829–832 (2022).
735 37. Schmidt, U., Weigert, M., Broaddus, C. & Myers, G. Cell Detection with Star-Convex Polygons. in
736 *Medical Image Computing and Computer Assisted Intervention – MICCAI 2018* (eds. Frangi, A. F.,
737 Schnabel, J. A., Davatzikos, C., Alberola-López, C. & Fichtinger, G.) 265–273 (Springer International
738 Publishing, Cham, 2018). doi:10.1007/978-3-030-00934-2_30.
739 38. Giese, W. EC-tracking-analysis. *GitHub* https://github.com/gerhardt-lab/ec-tracking-analysis/.
740 39. Giese, Wolfgang *et al.* Reconstructing stochastic cell population trajectories reveals regulators and
741 heterogeneity of endothelial flow-migration coupling driving vascular remodelling. *bioRxiv*
742 2023.05.30.542799 (2023) doi:10.1101/2023.05.30.542799.
743 40. Jin, Y. *et al.* Tyrosine-protein kinase Yes controls endothelial junctional plasticity and barrier
744 integrity by regulating VE-cadherin phosphorylation and endocytosis. *Nat. Cardiovasc. Res.* **1**, 1156–
745 1173 (2022).
746 41. Schindelin, J. *et al.* Fiji: an open-source platform for biological-image analysis. *Nat. Methods* **9**, 676–
747 682 (2012).
748 42. Narotamo, H., Silveira, M. & Franco, C. A. 3DVascNet: An Automated Software for Segmentation and
749 Quantification of Mouse Vascular Networks in 3D. *Arterioscler. Thromb. Vasc. Biol.* **44**, 1584–1600
750 (2024).

751 43. Ho, J., Tumkaya, T., Aryal, S., Choi, H. & Claridge-Chang, A. Moving beyond P values: data analysis
752 with estimation graphics. *Nat. Methods* **16**, 565–566 (2019).
753 44. Ravichandran, Y., Goud, B. & Manneville, J.-B. The Golgi apparatus and cell polarity: Roles of the
754 cytoskeleton, the Golgi matrix, and Golgi membranes. *Curr. Opin. Cell Biol.* **62**, 104–113 (2020).
755 45. Hamik, A. *et al.* Kruppel-like factor 4 regulates endothelial inflammation. *J. Biol. Chem.* **282**, 13769–
756 13779 (2007).
757 46. Villarreal, G. *et al.* Defining the regulation of KLF4 expression and its downstream transcriptional
758 targets in vascular endothelial cells. *Biochem. Biophys. Res. Commun.* **391**, 984–989 (2010).
759 47. Franco, C. A. *et al.* Dynamic Endothelial Cell Rearrangements Drive Developmental Vessel
760 Regression. *PLOS Biol.* **13**, e1002125 (2015).
761 48. Franco, C. A. *et al.* Non-canonical Wnt signalling modulates the endothelial shear stress flow sensor
762 in vascular remodelling. *eLife* **5**, e07727 (2016).
763 49. Baeyens, N. *et al.* Defective fluid shear stress mechanotransduction mediates hereditary
764 hemorrhagic telangiectasia. *J. Cell Biol.* **214**, 807–816 (2016).
765 50. Sugden, W. W. *et al.* Endoglin controls blood vessel diameter through endothelial cell shape
766 changes in response to haemodynamic cues. *Nat. Cell Biol.* **19**, 653–665 (2017).
767 51. Cait, J. *et al.* Podocalyxin is required for maintaining blood–brain barrier function during acute
768 inflammation. *Proc. Natl. Acad. Sci.* **116**, 4518–4527 (2019).
769 52. Debruin, E. J. *et al.* Podocalyxin Regulates Murine Lung Vascular Permeability by Altering Endothelial
770 Cell Adhesion. *PLOS ONE* **9**, e108881 (2014).
771 53. Fernández, D. *et al.* Control of cell adhesion and migration by podocalyxin. Implication of Rac1 and
772 Cdc42. *Biochem. Biophys. Res. Commun.* **432**, 302–307 (2013).
773 54. Nielsen, J. S. & McNagny, K. M. Novel functions of the CD34 family. *J. Cell Sci.* **121**, 3683–3692
774 (2008).

775 55. Fang, J. S. *et al.* Shear-induced Notch-Cx37-p27 axis arrests endothelial cell cycle to enable arterial
776 specification. *Nat. Commun.* **8**, 2149 (2017).
777 56. You, L.-R. *et al.* Suppression of Notch signalling by the COUP-TFII transcription factor regulates vein
778 identity. *Nature* **435**, 98–104 (2005).
779 57. Larrivée, B. *et al.* ALK1 Signaling Inhibits Angiogenesis by Cooperating with the Notch Pathway. *Dev.*
780 *Cell* **22**, 489–500 (2012).
781 58. Lobov, I. B. *et al.* The Dll4/Notch pathway controls postangiogenic blood vessel remodeling and
782 regression by modulating vasoconstriction and blood flow. *Blood* **117**, 6728–6737 (2011).
783 59. Phng, L.-K. & Gerhardt, H. Angiogenesis: A Team Effort Coordinated by Notch. *Dev. Cell* **16**, 196–208
784 (2009).
785 60. Akil, A. *et al.* Notch Signaling in Vascular Endothelial Cells, Angiogenesis, and Tumor Progression: An
786 Update and Prospective. *Front. Cell Dev. Biol.* **9**, 642352 (2021).
787 61. Jin, Z.-G. *et al.* Ligand-Independent Activation of Vascular Endothelial Growth Factor Receptor 2 by
788 Fluid Shear Stress Regulates Activation of Endothelial Nitric Oxide Synthase. *Circ. Res.* **93**, 354–363
789 (2003).
790 62. Horrillo, A., Porras, G., Ayuso, M. S. & González-Manchón, C. Loss of endothelial barrier integrity in
791 mice with conditional ablation of podocalyxin (Podxl) in endothelial cells. *Eur. J. Cell Biol.* **95**, 265–
792 276 (2016).
793 63. Hwang, H.-J. *et al.* The dipeptidyl peptidase-IV inhibitor inhibits the expression of vascular adhesion
794 molecules and inflammatory cytokines in HUVECs via Akt- and AMPK-dependent mechanisms. *Mol.*
795 *Cell. Endocrinol.* **405**, 25–34 (2015).
796 64. Shi, S. *et al.* Interactions of DPP-4 and integrin β1 influences endothelial-to-mesenchymal transition.
797 *Kidney Int.* **88**, 479–489 (2015).

798 65. Somanath, P. R., Malinin, N. L. & Byzova, T. V. Cooperation between integrin αvβ3 and VEGFR2 in
799 angiogenesis. *Angiogenesis* **12**, 177–185 (2009).
800 66. Crist, A. M. *et al.* Angiopoietin-2 Inhibition Rescues Arteriovenous Malformation in a Smad4
801 Hereditary Hemorrhagic Telangiectasia Mouse Model. *Circulation* **139**, 2049–2063 (2019).
802 67. Cui, X. *et al.* Venous Endothelial Marker COUP-TFII Regulates the Distinct Pathologic Potentials of
803 Adult Arteries and Veins. *Sci. Rep.* **5**, 16193 (2015).
804 68. Augustin, H. G., Young Koh, G., Thurston, G. & Alitalo, K. Control of vascular morphogenesis and
805 homeostasis through the angiopoietin–Tie system. *Nat. Rev. Mol. Cell Biol.* **10**, 165–177 (2009).
806 69. Oh, H. *et al.* Hypoxia and Vascular Endothelial Growth Factor Selectively Up-regulate Angiopoietin-2
807 in Bovine Microvascular Endothelial Cells*. *J. Biol. Chem.* **274**, 15732–15739 (1999).
808 70. Kampen, S. J. van *et al.* Controlled Induction of ALK1 in ACVRL1-null hiPSC-derived Endothelial Cells
809 Provides Insight into Organ-Restricted AVMs in HHT. 2025.08.22.671484 Preprint at
810 https://doi.org/10.1101/2025.08.22.671484 (2025).
811 71. Zhou, X. *et al.* ANG2 Blockade Diminishes Proangiogenic Cerebrovascular Defects Associated With
812 Models of Hereditary Hemorrhagic Telangiectasia. *Arterioscler. Thromb. Vasc. Biol.* **43**, 1384–1403
813 (2023).
814 72. Lobov, I. B., Brooks, P. C. & Lang, R. A. Angiopoietin-2 displays VEGF-dependent modulation of
815 capillary structure and endothelial cell survival in vivo. *Proc. Natl. Acad. Sci.* **99**, 11205–11210
816 (2002).
817 73. Sack, K. D., Kellum, J. A. & Parikh, S. M. The Angiopoietin-Tie2 Pathway in Critical Illness. *Crit. Care*
818 *Clin.* **36**, 201–216 (2020).
819 74. Rochon, E. R., Menon, P. G. & Roman, B. L. Alk1 controls arterial endothelial cell migration in
820 lumenized vessels. *Development* **143**, 2593–2602 (2016).

821

822 **Main figure legends:**

823 **Figure 1: differential transcriptomic changes in ECs under flow**

824 a. Experimental schematic- HUVECs treated with siRNA against ALK1 or SMAD4 are exposed
825 to 4 or 16 hours of laminar FSS 0.6 Pa (LSS hereafter).
826 b. Principal component analysis of RNAseq samples. Dashed circles group samples by flow
827 duration. n=3 independent experiments.
828 c. Panel plot of select biological processes, significantly (adj. P-value<0.05) enriched in
829 *siSMAD4*-treated samples vs *siALK1*-treated samples after 4 and/or 16h of LSS. The length of
830 the rectangle is the effect size (area under the curve or AUC, see Figure 1d). In red and blue
831 are the fraction of significantly up- or down-regulated genes from that gene set. AUC_{min}=0,
832 AUC_{max}=1. Vertical lines represent threshold value (AUC=0.65) for each column.
833 d. Evidence plots of GO Terms representing differential regulation in two biological
834 processes. X-axis is the list of all genes sorted by their p-value. Y-axis is the cumulative
835 fraction. Light blue and light red colors represent significant down– or up-regulation,
836 respectively.
837 e. Volcano plots of differentially expressed genes in *siSMAD4* treated samples vs *siALK1*
838 treated samples, significance cut-off - Log2FC of at least 0.5. Select genes of interest are color-
839 annotated. SMAD4 and ACVRL1 are annotated in pink to confirm knockdown.

840 **Figure 2: BMP pathway activation and cell polarity under flow**

841 a. pSMAD159 staining of HUVECs after exposure to LSS. Control cells have an initial
842 activation of the BMP pathway which goes down over time, while *siSMAD4* cells have
843 constant BMP activity and siALK1 cells don't have BMP pathway activation. Scale bar 100µm.
844 b. and c. Quantification of nuclear pSMAD159 signal , normalized to cytosolic signal at 0.6
845 and 1.8 Pa. Statistical analysis was performed using Welch's test, n≥30 images per condition,
846 from at least 3 independent experiments (b) and n=20 from 2 independent experiments (c).
847 d. Rose diagrams depicting the Nuclei-Golgi polarity of *siCTRL*-, *siSMAD4*- and *siALK1*-treated
848 ECs exposed to LSS or HSS (1.8 Pa) for 4 and 16 hours. The red arrow points towards the mean
849 direction of polarization and its length represents the polarity index (PI), which is an indicator

850 for the variance of the distribution; the black line represents the signed polarity index (V-
851 score). Data underneath each rose diagram depict the total number of cells/images (N),
852 number of experiments (n) and numerical values for PI and V-Score.
853 e. and f. Graphical representation of V-score values from d for LSS and HSS (f), each data
854 point representing mean V-Score of an individual image. Box plots display median values
855 along with the standard deviation. Statistical analysis was performed using Welch's test.

856 **Figure 3: Endothelial response to FSS via KLF4 signaling and morphological changes**

857 a. Analysis of KLF4 mRNA expression after exposure to LSS in Log2FC scale. Static samples are
858 relative to wild-type static, flow samples are relative to static samples for the same siRNA
859 condition. *siSMAD4*-treated samples have higher upregulation of KLF4 while *siALK1*-treated
860 samples have a lower upregulation of KLF4, indicative of their disturbed flow sensation.
861 Adjusted p-values (padj) are indicated. n=3 independent experiments.
862 b. Evidence plot of biological process "response to fluid shear stress", comparing *siSMAD4*-
863 treated samples relative to *siALK1*-treated samples after 16h of LSS. X-axis is the list of all
864 genes sorted by their p-value. Y-axis is the cumulative fraction. Light blue and light red colors
865 represent significant down– or up-regulation.
866 c. Quantification of nuclear KLF4 signal, normalized to cytosolic signal. Statistical analysis was
867 performed using the Welch's test, n=40 images per condition, from 4 independent
868 experiments.
869 d. Representative immunofluorescence staining of VEcadherin after 16h of LSS (top) and the
870 corresponding cell orientation plots (bottom). Scale bar 100µm.
871 e. Quantification of cell orientation V-score values. Box blots display median values and
872 standard deviation. *siSMAD4*-treated cells orient themselves better parallel to flow than
873 *siCTRL*-treated cells, and *siALK1*-treated cells form subpopulations that have different cell
874 orientation. Statistical analysis was performed using Welch's test, n=4 independent
875 experiments with 10 images per experiment.
876 f. Cell area analysis in μm^2 and g. Cell elongation as ratio of major over minor axes of ECs after
877 16h of LSS. *siSMAD4*-treated cells are significantly bigger than *siCTRL*-treated cells; *siALK1*-

878 treated cells are not bigger than *siCTRL*-treated cells but are less variable in size and shape.
879 Statistical analysis using Welch's test, n=4 independent experiments with 10 images per
880 experiment.

881 **Figure 4: Endothelial migration *in vitro***

882 a. Bootstrapped trajectory plots of initial 5 hours of migration for all conditions, 100 tracks per
883 replicate, and 400 tracks per condition. Starting point of each cell trajectory has been normalized
884 to start from (0, 0). Color intensity map represents scale of parallel migration velocity with flow
885 (blue) to against flow (red).
886 b. Representative track images from individual samples of the initial 16 hours of migration.
887 Spatial position of each track is kept.
888 c. Mean migration velocity of *siCTRL*-, *siSMAD4*- or *siALK1*-treated HUVECs, parallel to flow
889 direction (top) or overall (bottom). n=4 individual experiments per siRNA treatment.
890 d. Mosaic migration setup. Cells are separately labeled with CellTracker Green (green cells) or
891 Red (magenta cells) and mixed before seeding in flow slides.
892 e. Bootstrapped trajectory plots with normalized starting position of the green (top) and
893 magenta (bottom) cells in each co-culture, from t=10 to t=20 hours. 100 tracks per replicate per
894 color, from n=4 independent experiments. Color intensity map represents scale of migration
895 velocity with flow (blue) to against flow (red).
896 f. and g. Mean migration velocity of *siCTRL*-treated cells when co-cultured either with
897 themselves (*siCTRL*_mosaic, light pink/green curve), or with *siSMAD4*- or *siALK1*-treated cells
898 (*siCTRL_siSMAD4*, *siCTRL_siALK1*, respectively), parallel to flow direction (f) or overall (g). Cells
899 were labeled with CellTracker Green or Red (Thermofisher) and seeded together in 1:1 ratio. n=4
900 independent experiments. Red rectangles represent the time window of trajectory plot analysis.

901 Statistical analysis: mean difference plots of the velocity parallel to flow (f) or total velocity (g),
902 generated using estimation statistics. Both groups of *siCTRL*-treated cells (green+red) migrate
903 similarly when cultured together. *siCTRL*-treated cells (green) migrate at a similar speed when
904 cultured with *siALK1*-treated cells, or faster parallel to flow when cultured with *siSMAD4*-treated
905 cells within the measured time interval (red dashed rectangles).

906 **Figure 5: *In vivo* EC population distribution analysis**

907 a. Tamoxifen injection regimen. Single 0.75ug injection of T-OH at P5 to induce mosaic gene
908 deletion and subsequent expression of GFP, collection at P8 and P15. Number of retinae
909 collected per condition: P8_CTRL^{mTmG}=8; P15_CTRL^{mTmG}=8; P8_Smad4^{mTmG}=8;
910 P15_Smad4^{mTmG}=14; P8_Alk1^{mTmG}=10; P15_Alk1^{mTmG}=6;
911 b. Representative microscopy images of P8 retina GFP, IB4 and merged channels. Scale bar -
912 500µm.
913 c. Representative images of retina sections at both time points for CTRL^{mTmG} (left), Smad4^{mTmG}
914 (middle) and Alk1^{mTmG} (right) conditions; arteries – a and veins – v. Scale bar - 250µm.
915 Resulting KDE plots for P8 and P15 for each condition on the bottom.
916 d. Mean difference statistical analysis of P15 GFP+EC percentage within the artery relative to
917 P8.
918 e. Mean difference statistical analysis of P15 GFP+EC percentage within the venous bed relative
919 to P8.
920 f. Mean difference statistical analysis of P15 GFP+EC percentage within the arterial bed relative
921 to P8.

922 **Figure 6: in vivo regression analysis in postnatal retina**

923 a. Tamoxifen injection regimen for Smad4^{iECKO} and Alk1^{iECKO}, respectively. $N_{Smad4\ f/f}$=6, N_{Smad4}
924 $_{iECKO}$=8, $N_{Alk1\ f/f}$=7, $N_{Alk1\ iECKO}$=8.
925 b. Representative grayscale and merge of maximum intensity projections of CD31 channel and
926 Col IV channel of Alk1 littermate control retina. Dark blue triangles indicate a regression
927 event, which is defined by partial or total absence of CD31 signal within a vessel while ColIV
928 signal is present. Scale bar 100µm.
929 c. Representative images of immunofluorescent staining of CD31 (green) and Collagen Type 4
930 (magenta) in P6 littermate controls (top) and mutated (bottom) retinae. Blue rectangles
931 annotate zoomed in sections on the right. Dark blue unfilled triangles mark regression events,
932 filled triangles mark anastomosis events. AVMs are highlighted in yellow dashed lines. Size
933 marker 250µm in main images, 100µm in zoomed in images; v - vein, a - artery.

934 d. Regression frequency, presented by number of regression events per 100 CD31+ branching
935 points. Number of branching points is extracted from the 3DVascNet software for both CD31
936 and Col IV channels. Regression events are counted within a region of interest (ROI) which is
937 also used to determine the number of branching points. Two-sided non-parametric Mann
938 Whitney test was used to determine statistical significance. Data are represented as mean ±
939 SEM.
940 e. Branching points' density (# branching points/ROI volume) and f. vessel density (vessel
941 volume/ROI volume x100%) ratios in littermate controls (full-color bars) and KO retinae
942 (dotted bars). Two-sided non-parametrical Mann Whitney test was used to determine
943 statistical significance. Data are represented as mean ± SEM.

944

945 **Supplementary figure legends:**

946 **Supplementary figure 1**:

947 1.1 Knockdown verification of SMAD4, ALK1. Top – qPCR analysis of *siCTRL* (black), *siSMAD4*
948 (blue), *siALK1* (magenta), *siDouble* (lime), 48h post siRNA treatment. Log2FC values represent
949 relative expression to b-actin. N=3 independent experiments. Bottom – Western blot analysis
950 of *siCTRL*, *siSMAD4* and *siALK1* with representative images of blots, 48h post siRNA
951 treatment. Bands normalized to GAPDH; n=3 independent experiments.
952 1.2 Full panel plot of GO_BP of *siSMAD4* vs. *siALK1* in static, 4h and 16h of LSS. GO_BPs are
953 clustered according to their enrichment in the different flow conditions: Cluster I –
954 enrichment in all flow conditions; Cluster II – enrichment in static only; Cluster III –
955 enrichment in 4h LSS only; Cluster IV – enrichment in 16h LSS only; Cluster V – enrichment in
956 both 4h and 16h LSS; Cluster VI – enrichment in static and a 4h LSS **OR** 16h LSS.
957 1.3 Expression patterns of individual genes over time (RNAseq data). Y axis is Log2FC scale, X axis
958 are flow conditions. Expression patterns of a. PODXL, b. DPP4, c. ITGAV, d. ITGB3, e. CDKN1B
959 (p27), f. GJA4 (Cx37), g. BMP4, h. NR2F2, i. DLL4, j. HEY1, k. HEY2, l. ANGPT2, m. TEK (Tie2).
960 *siCTRL* – black; *siSMAD4* – blue; *siALK1* – magenta.

961

962

963 **Supplementary figure 2**:

964 Representative pSMAD159 immunofluorescence images of HUVECs after exposure to HSS
965 (1.8Pa). Scale bar 100µm.

966 **Supplementary figure 3:**

967 a. Representative KLF4 immunofluorescence images of HUVECs after exposure to static, 4h and
968 16h LSS conditions. Scale bar 100µm.
969 b. Representative VEcad staining of HUVECs after exposure to static, 4h and 16h of LSS
970 conditions. Scale bar 100µm.
971 c. –e Mean difference statistical analysis of cell area (c), cell elongation (d) and cell orientation
972 (e) of *siCTRL-*, *siSMAD4-* and *siALK1*-treated cells at static, 4h and 16h of LSS. The further away
973 the difference histogram is from the control group line (0.0), the higher the significance.

974 **Supplementary figure 4**:

975 Mosaic EC population shift *in vivo*.
976 a. Analysis overview: two-dimensional masks of retina outline, arteries and veins in flat-
977 mounted retinas, result in a 2D map. Each GFP+ EC' coordinates are based on its location relative
978 to the vein(0.0) and artery (1.0) and the radial distance from the optic nerve to the sprouting
979 front. Kernel Density Estimate (KDE) plots represent the cumulative location of all GFP+ EC across
980 all retinae for each condition.
981 b. Density histograms of CTRL^{mTmG} (black), Smad4^{mTmG} (blue) and Alk1^{mTmG} (magenta) in overlay,
982 describing GFP+EC distance relative to artery at P8 (left) and P15 (right).
983 c. Mean difference statistical analysis of P8 (left) and P15 (right) GFP+EC distribution in the 75th
984 percentile on the vein-artery axis, equivalent to the peri-arterial capillary bed.
985 d. Mean difference statistical analysis of P8 (left) and P15 (right) GFP+ EC distribution the 90th
986 percentile on the vein-artery axis, equivalent to the arteries and immediate surrounding vessels.

987 **Supplementary figure 5**:

988 Grayscale Col IV and CD31 channel images of enlarged sections of Figure 6. Scale bar 100 µm.

989 **Supplementary movies:**

990 Live imaging of endothelial migration under flow.

991 **1.** Representative time lapse imaging of HUVECs labeled with SPY505 and exposed to LSS for 48h.

992 a. siCTRL; b. siSMAD4; c. siALK1. Frame interval – 7.5 minutes.

993 **2.** Representative time lapse imaging of HUVECs labeled with CellTracker Green (siCTRL) and

994 CellTracker Red (siCTRL/siSMAD4/siALK1) and exposed to LSS for 62h. a. siCTRL mosaic (green +

995 red); b. siCTRL green+siSMAD4 red; c. siCTRL green+siALK1 red.

Figure 1

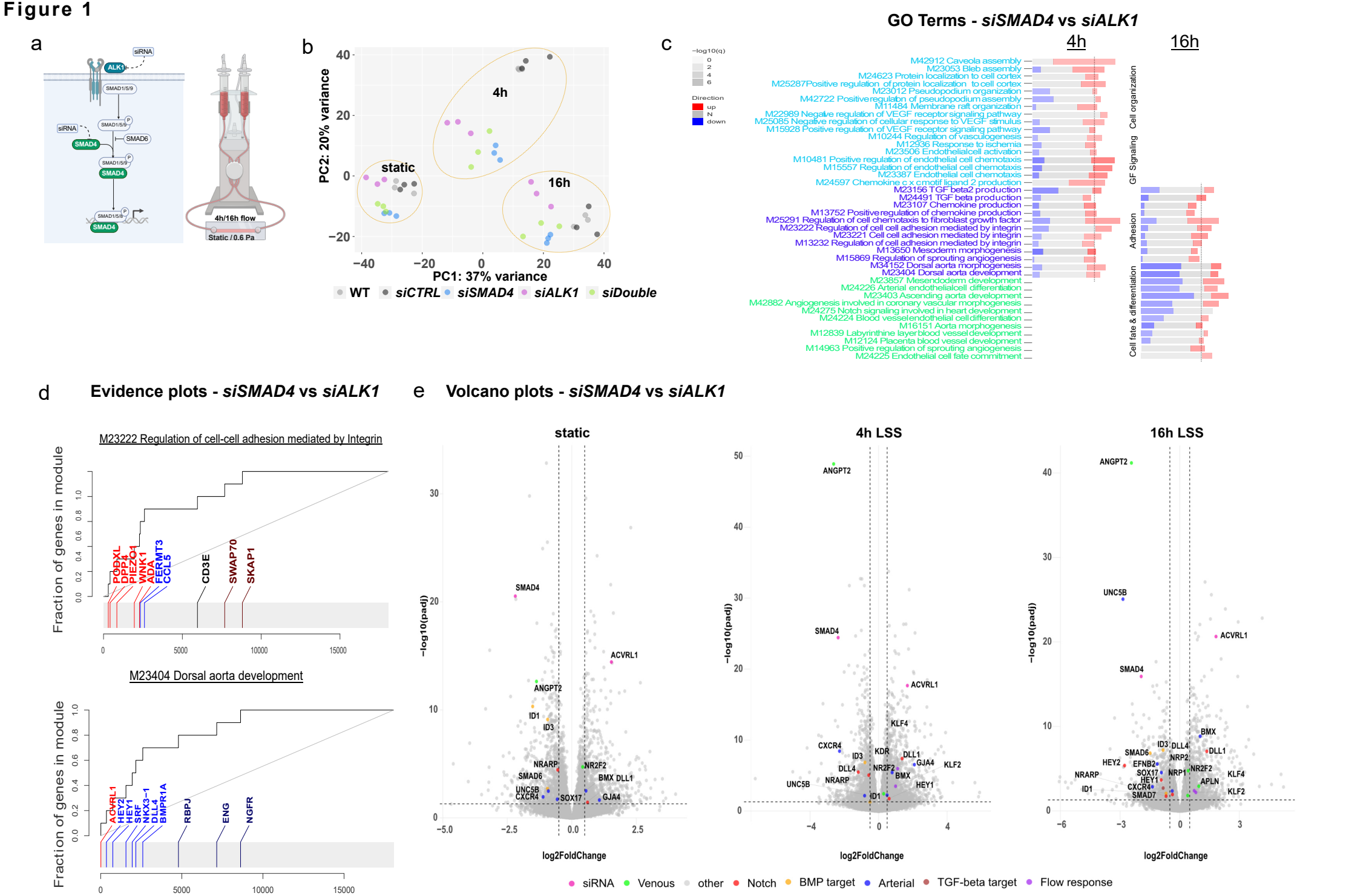
a
siRNA
ALK1
SMAD1/5/9
SMAD6
SMAD4
4h/16h flow
Static / 0.6 Pa
b
PC2: 20% variance
PC1: 37% variance
static
4h
16h
WT
siCTRL
siSMAD4
siALK1
siDouble
c
GO Terms - siSMAD4 vs siALK1
4h
16h
Cell organization
GF Signaling
Adhesion
Cell fate & differentiation
d
Evidence plots - siSMAD4 vs siALK1
M23222 Regulation of cell-cell adhesion mediated by Integrin
M23404 Dorsal aorta development
Fraction of genes in module
e
Volcano plots - siSMAD4 vs siALK1
static
4h LSS
16h LSS
−log10(padj)
log2FoldChange
siRNA
Venous
other
Notch
BMP target
Arterial
TGF-beta target
Flow response

Figure 2

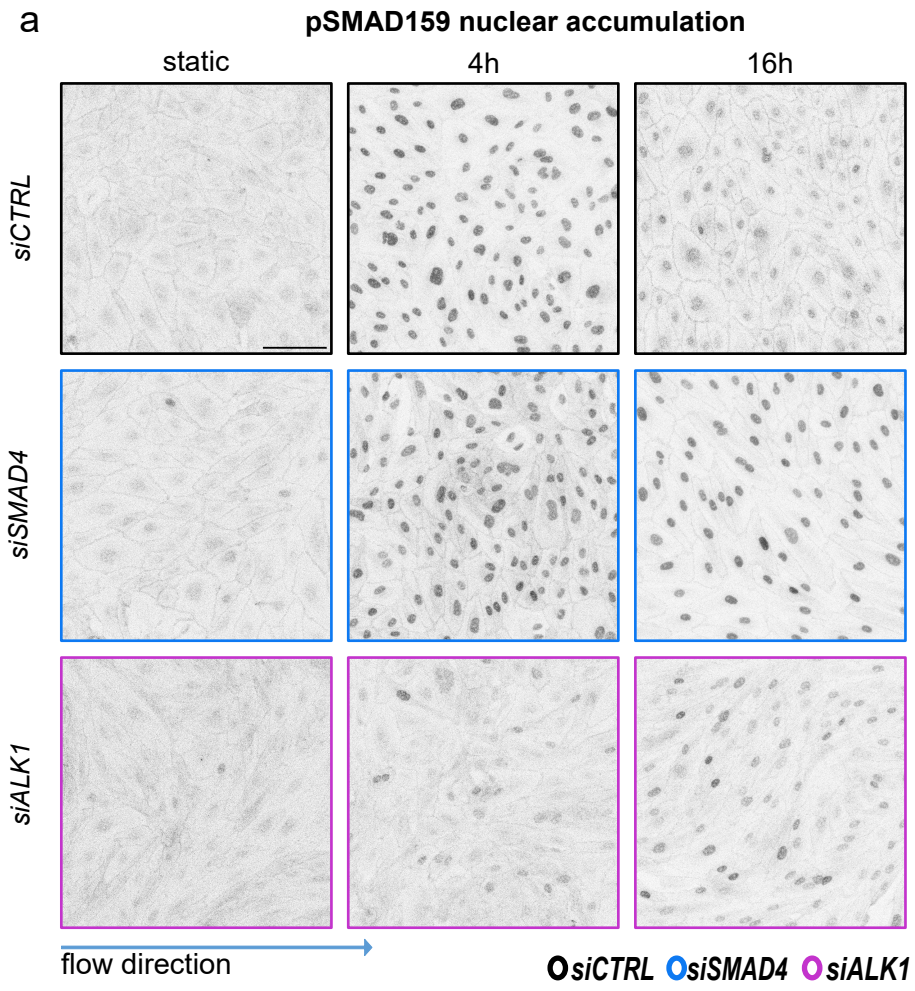
a
pSMAD159 nuclear accumulation
static
4h
16h
siCTRL
siSMAD4
siALK1
flow direction
siCTRL siSMAD4 siALK1

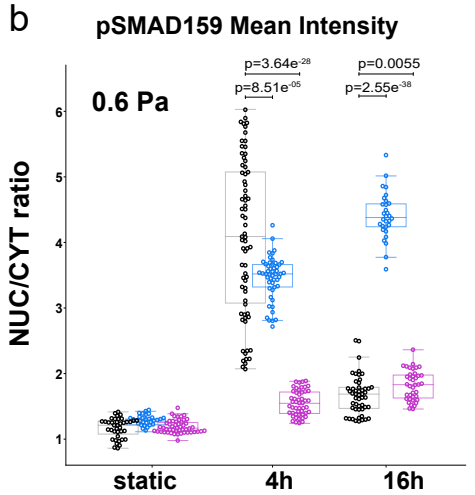
b
pSMAD159 Mean Intensity
0.6 Pa
NUC/CYT ratio
p=3.64e-28
p=8.51e-05
p=0.0055
p=2.55e-38
static
4h
16h

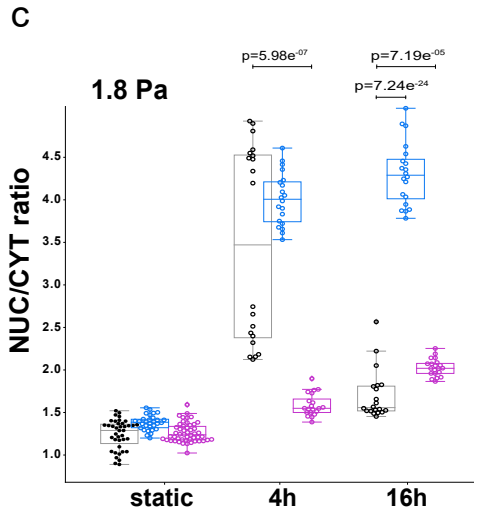
c
1.8 Pa
NUC/CYT ratio
p=5.98e-07
p=7.19e-05
p=7.24e-24
static
4h
16h

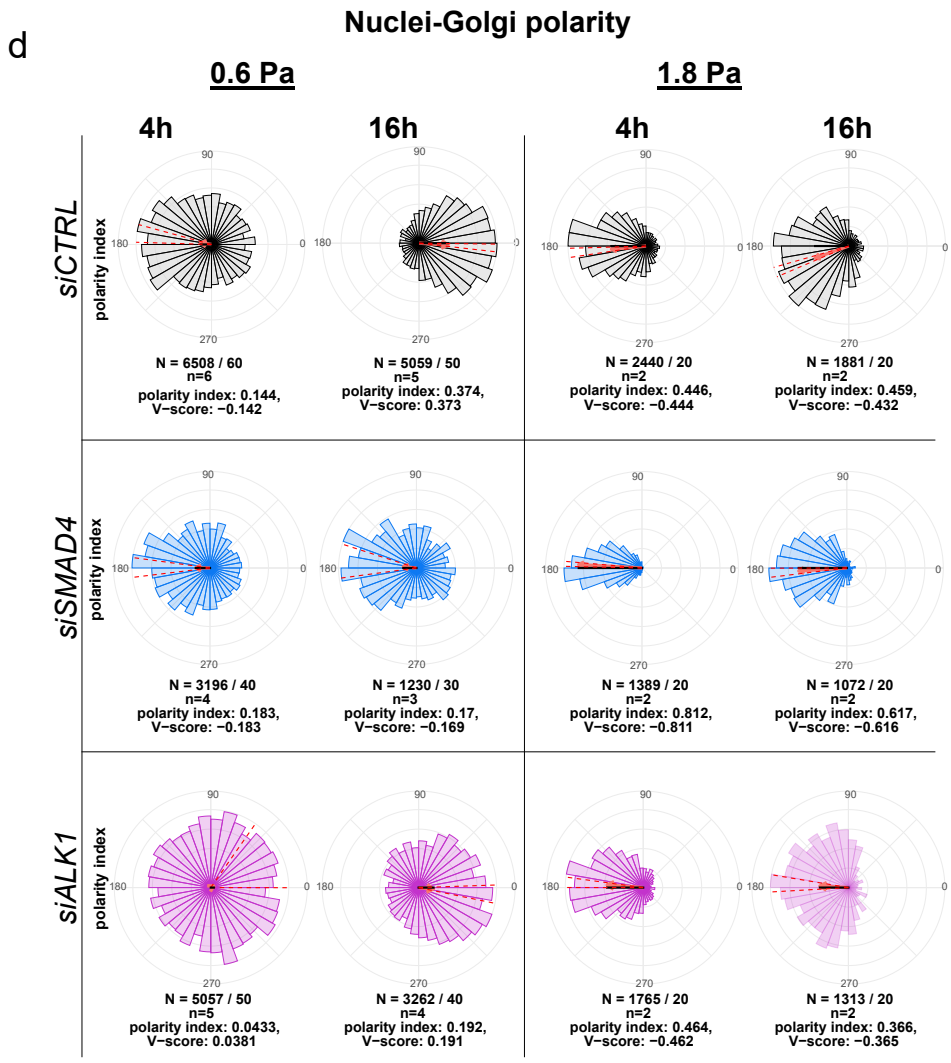
d
Nuclei-Golgi polarity
0.6 Pa
1.8 Pa
4h
16h
siCTRL
siSMAD4
siALK1
polarity index
N = 6508 / 60
n=6
polarity index: 0.144,
V−score: −0.142
N = 5059 / 50
n=5
polarity index: 0.374,
V−score: 0.373
N = 2440 / 20
n=2
polarity index: 0.446,
V−score: −0.444
N = 1881 / 20
n=2
polarity index: 0.459,
V−score: −0.432
N = 3196 / 40
n=4
polarity index: 0.183,
V−score: −0.183
N = 1230 / 30
n=3
polarity index: 0.17,
V−score: −0.169
N = 1389 / 20
n=2
polarity index: 0.812,
V−score: −0.811
N = 1072 / 20
n=2
polarity index: 0.617,
V−score: −0.616
N = 5057 / 50
n=5
polarity index: 0.0433,
V−score: 0.0381
N = 3262 / 40
n=4
polarity index: 0.192,
V−score: 0.191
N = 1765 / 20
n=2
polarity index: 0.464,
V−score: −0.462
N = 1313 / 20
n=2
polarity index: 0.366,
V−score: −0.365

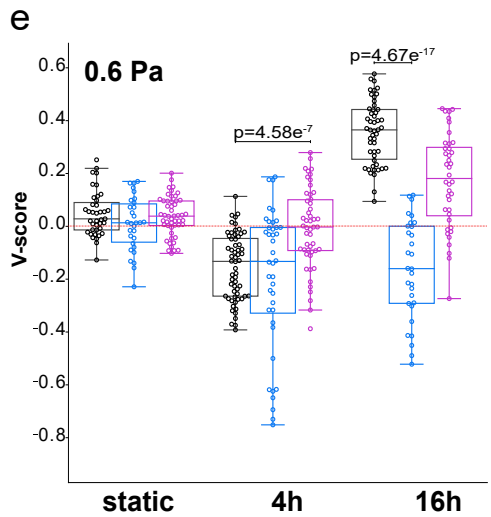
e
0.6 Pa
V-score
p=4.58e-7
p=4.67e-17
static
4h
16h

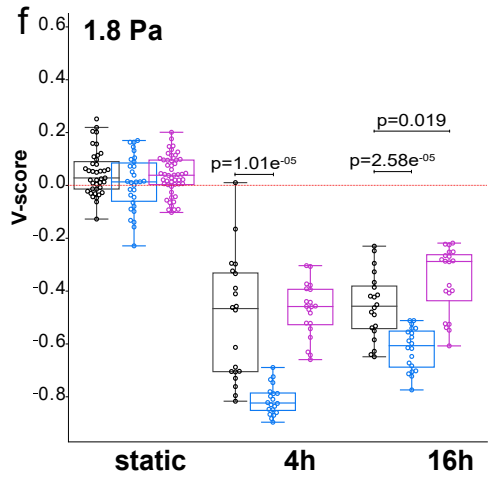
f
1.8 Pa
V-score
p=1.01e-05
p=2.58e-05
p=0.019
static
4h
16h

Figure 3

EC Response to fluid shear stress

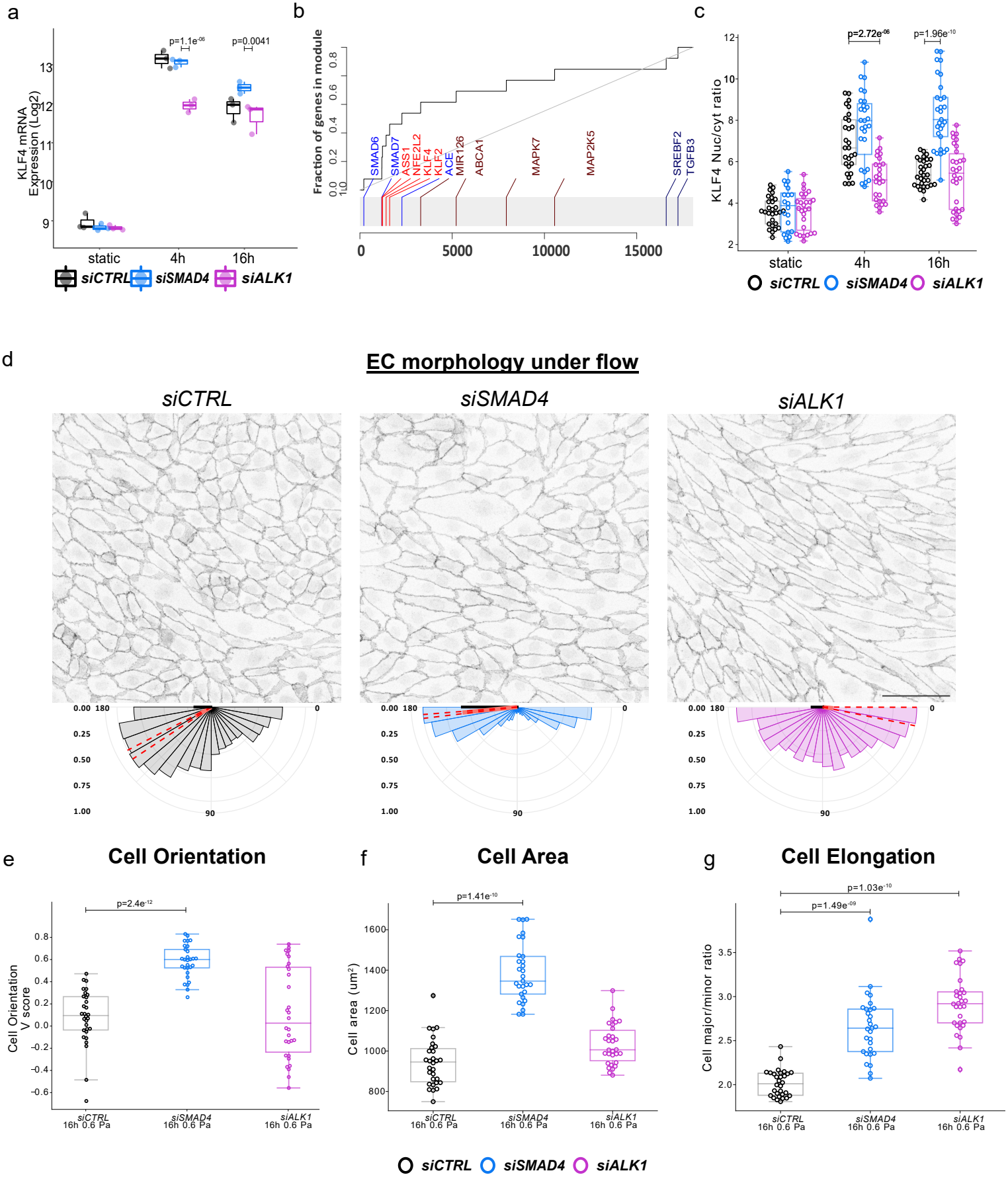

Figure 4

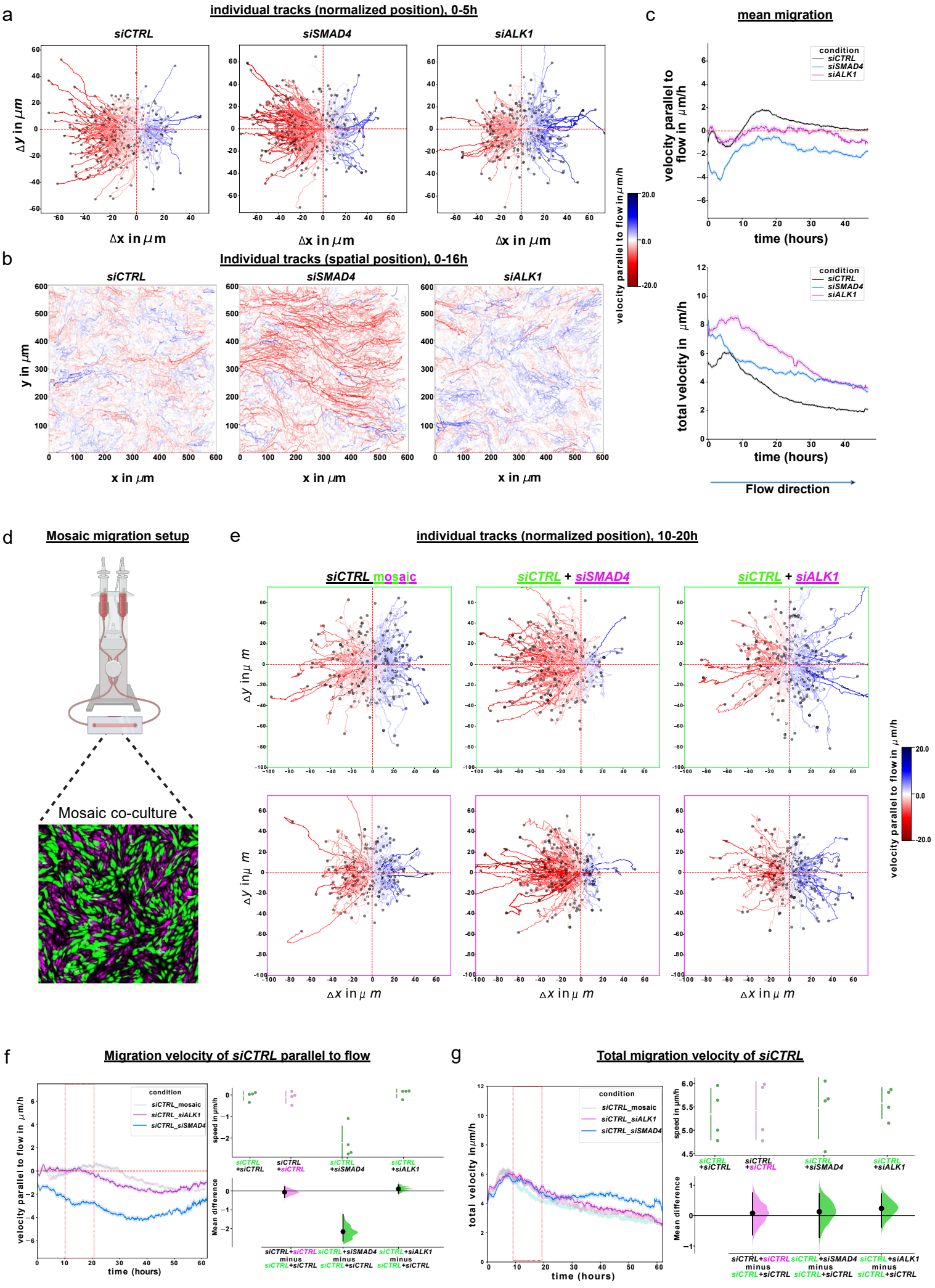
a
individual tracks (normalized position), 0-5h
siCTRL
siSMAD4
siALK1
Δy in μm
Δx in μm
velocity parallel to flow in μm/h
20.0
0.0
-20.0
b
Individual tracks (spatial position), 0-16h
y in μm
x in μm
c
mean migration
condition
siCTRL
siSMAD4
siALK1
velocity parallel to flow in μm/h
total velocity in μm/h
time (hours)
Flow direction
d
Mosaic migration setup
Mosaic co-culture
e
individual tracks (normalized position), 10-20h
siCTRL mosaic
siCTRL + siSMAD4
siCTRL + siALK1
Δy in μ m
Δx in μ m
velocity parallel to flow in μ m/h
f
Migration velocity of siCTRL parallel to flow
condition
siCTRL_mosaic
siCTRL_siALK1
siCTRL_siSMAD4
velocity parallel to flow in μm/h
time (hours)
speed in μm/h
Mean difference
siCTRL +siCTRL
siCTRL +siSMAD4
siCTRL +siALK1
siCTRL+siCTRL minus siCTRL+siCTRL
siCTRL+siSMAD4 minus siCTRL+siCTRL
siCTRL+siALK1 minus siCTRL+siCTRL
g
Total migration velocity of siCTRL
total velocity in μm/h

Figure 5

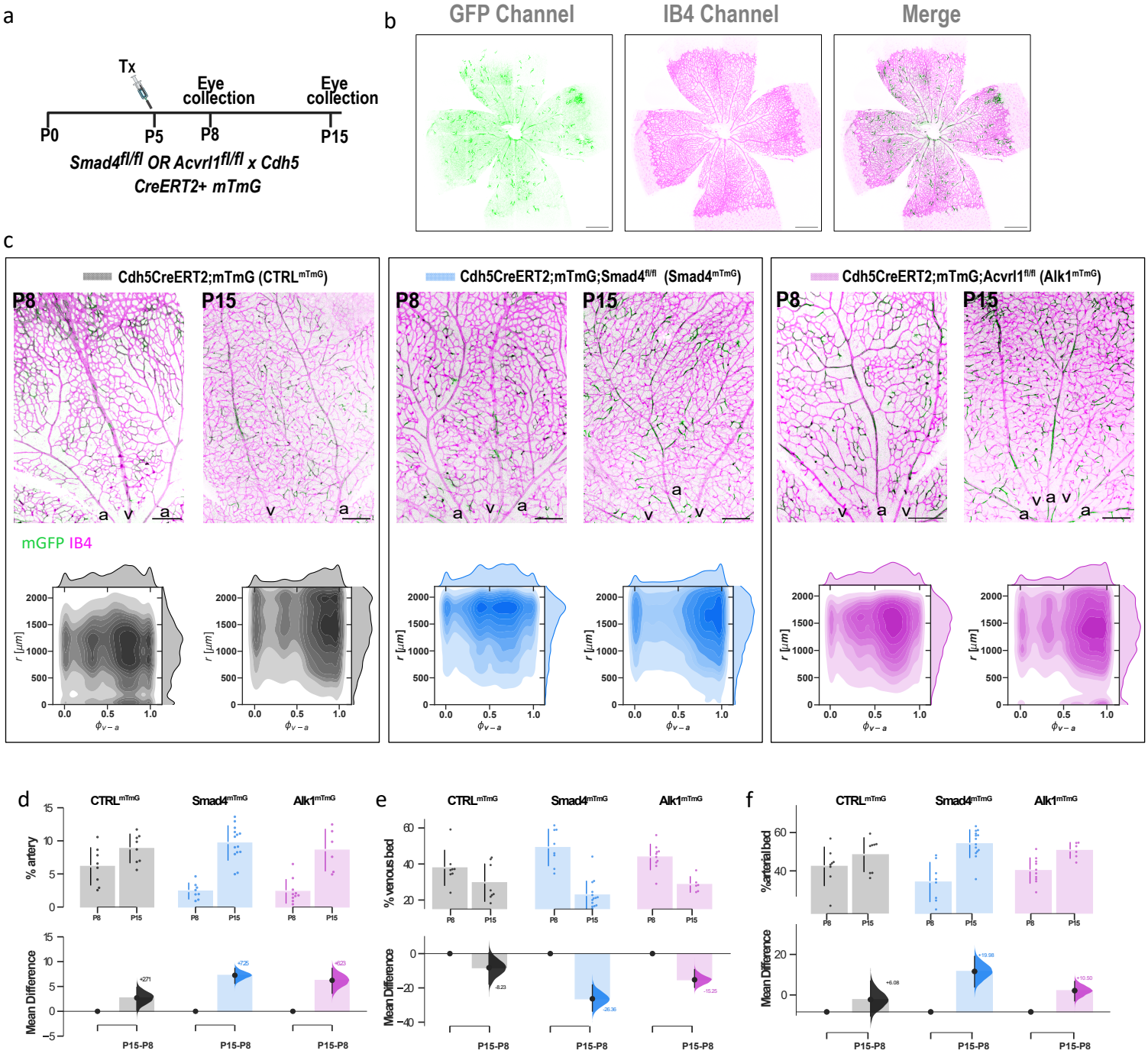

a
Tx
Eye collection
Eye collection
P0
P5
P8
P15
Smad4fl/fl OR Acvrl1fl/fl x Cdh5 CreERT2+ mTmG
b
GFP Channel
IB4 Channel
Merge
c
Cdh5CreERT2;mTmG (CTRLmTmG)
Cdh5CreERT2;mTmG;Smad4fl/fl (Smad4mTmG)
Cdh5CreERT2;mTmG;Acvrl1fl/fl (Alk1mTmG)
P8
P15
mGFP IB4
r [μm]
ϕv−a
d
CTRLmTmG
Smad4mTmG
Alk1mTmG
% artery
Mean Difference
P15-P8
e
% venous bed
f
% arterial bed

Figure 6

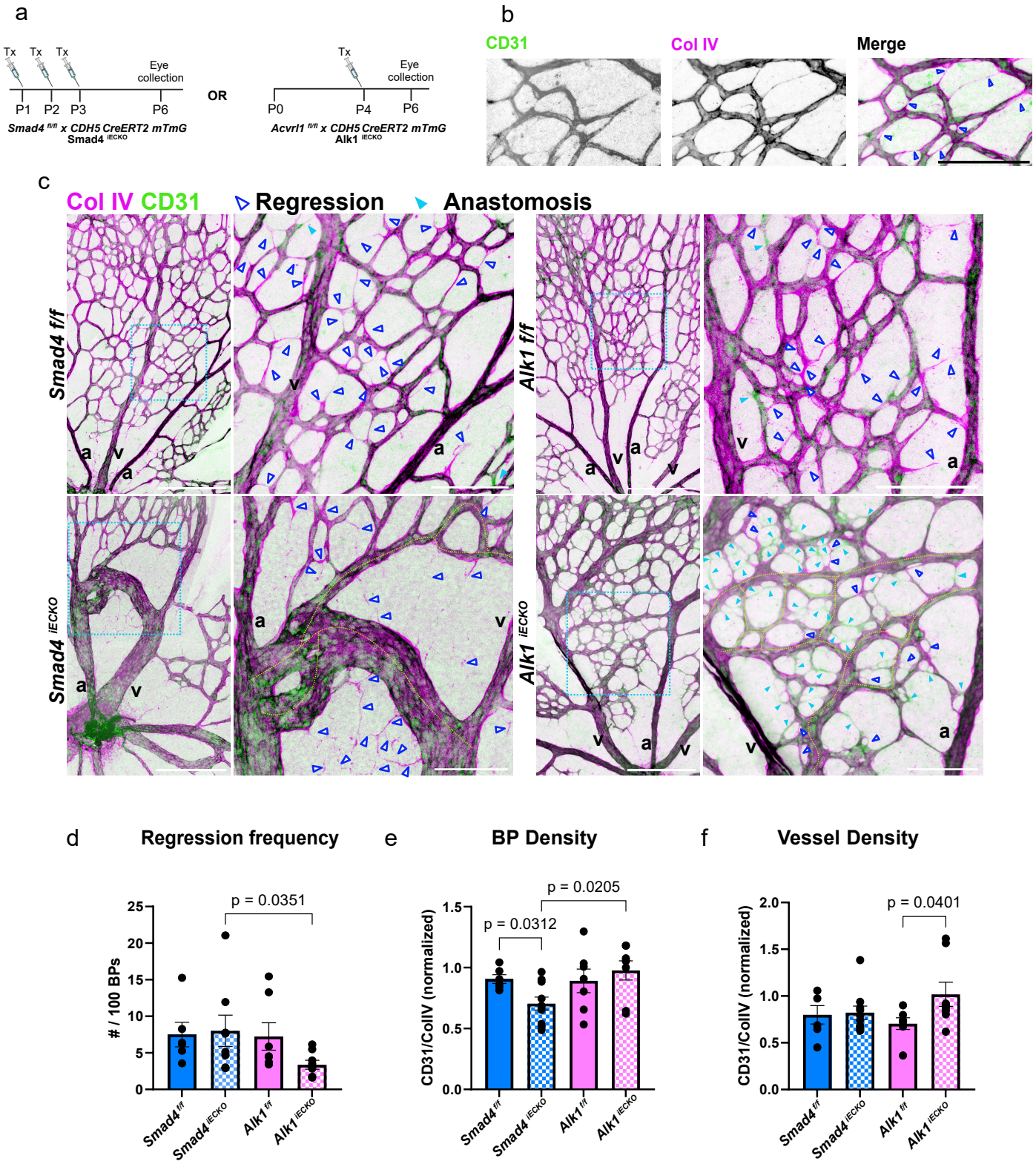
a
Tx
Tx
Tx
Eye collection
P1
P2
P3
P6
Smad4 f/f/f x CDH5 CreERT2 mTmG
Smad4 iECKO
OR
Tx
Eye collection
P0
P4
P6
Acvrl1 f/f/f x CDH5 CreERT2 mTmG
Alk1 iECKO
b
CD31
Col IV
Merge
c
Col IV CD31
Regression
Anastomosis
Smad4 f/f
Smad4 iECKO
Alk1 f/f
Alk1 iECKO
a
v
d
Regression frequency
# / 100 BPs
p = 0.0351
Smad4 f/f
Smad4 iECKO
Alk1 f/f
Alk1 iECKO
e
BP Density
CD31/ColIV (normalized)
p = 0.0312
p = 0.0205
f
Vessel Density
CD31/ColIV (normalized)
p = 0.0401